Studying evaporation from Ottawa sand with mixed wettabilities under a simulated solar flux with forced convection: Experimental apparatus design and evaporation rates

by

Dylan Paap

B.S., Concordia University, Nebraska, 2020

A THESIS

submitted in partial fulfillment of the requirements for the degree

MASTER OF SCIENCE

Alan Levin Department of Mechanical and Nuclear Engineering
Carl R. Ice College of Engineering

KANSAS STATE UNIVERSITY
Manhattan, Kansas

2023

Approved by:

Major Professor
Dr. Melanie M. Derby

Copyright

Abstract

The primary source of water for crops and livestock in the United States Central High Plains is irrigation from the Ogallala Aquifer [1], supplying 30% of the water used in the United States' irrigated agriculture in 2015 [2]. Due to the semi-arid climate of this region, limited rainfall (e.g., 33-74 cm of precipitation [3]) contributes to watering crops, thereby resulting in water scarcity. Reducing the evaporation from soil is one approach to conserving water and improving water use efficiency.

In this study, a soil-water evaporation test section was designed and constructed to study evaporation from Ottawa sand with constant air flow above and below the sand layer. A simulated solar flux was applied to the sand, while varying soil wettability (e.g., all hydrophilic, 12% hydrophobic sand concentrated in a layer, and 12% hydrophobic sand evenly mixed). Prior to entering the sand test section, compressed air was dried in a desiccator and then split in two flows before flowing through the 5.7-cm-depth, 22.8-cm-wide, and 83.8-cm-long test section, with one air stream flowing above the 5.7-cm-thick sand layer and the other below and, subsequently, flowing through the moist sand layer. The air temperature, pressure, and relative humidity were measured at the inlets and outlet of the test section to measure the change in moisture and, therefore, water content removed from the sand via evaporation. Using inlet air mass flow rates of air of approximately 2E-4 kg/s for each inlet, air temperatures of 28–31 °C, and dry air (i.e. 0–2% RH), an applied solar heat flux of 112±20 W/m^2, and steady state exit air temperatures of approximately 27 °C, evaporation rates were measured for three cases: 1) a 5.7-cm thick layer of hydrophilic Ottawa sand; 2) a 5.7-cm-thick layer with 12% hydrophobic content consisting of a 0.7-cm-layer of hydrophobic sand buried 1.8 cm below the surface of hydrophilic sand, termed

hydrophobic layer; and 3) a 5.7-cm-thick layer with mixed wettabilities consisting of 12% hydrophobic sand mixed into hydrophilic sand, termed hydrophobic mixture.

Evaporation from porous media often occurs at a high, constant-rate driven by capillary flow for higher saturations. This is followed by a falling-rate, and slow-rate evaporation driven by vapor diffusion for lower saturations. The saturation percentage of the sand was measured via a gravimetric approach during evaporation of the three experiments.

The evaporation rate of water for each experiment began at a quasi-constant rate: approximately 8.7E-6 kg/s to 9.6E-6 kg/s for the all hydrophilic case, 8.6 E-6 kg/s to 8.9 E-6 kg/s for the hydrophobic layer, and 8.1E-6 kg/s to 9.0E-6 kg/s for the hydrophobic mixture. The hydrophilic experiment entered the falling-rate of evaporation at 12% saturation, the hydrophobic layer entered the falling-rate of evaporation at 20% saturation, and the hydrophobic mixture entered the falling-rate of evaporation at 24% saturation.

The change in onset of the falling-rate of evaporation led to more experimental measurements required to complete the entire saturation curve for the hydrophobic experiments. With each experiment beginning at approximately 40% saturation, the hydrophilic experiment took 17 trials to complete, the hydrophobic layer took 20 trials to complete, and the hydrophobic mixture took 26 trials to complete. The hydrophobic mixture took the most trials to complete the saturation curve and had the shortest constant-rate period of evaporation. The addition of hydrophobic Ottawa sand to hydrophilic Ottawa sand reduced the evaporation rates at higher saturation percentages, thereby increasing water retention compared to all hydrophilic Ottawa sand.

Effective thermal conductivities were calculated for each experiment at three locations within the sand layer. Effective thermal conductivities were found to be higher than the

expected values. This was attributed to uneven moisture distribution and thermal losses by convection and conduction through the test section walls. The evaporation flux was measured to be up to 12 times higher than the diffusion flux calculated throughout each experiment. This suggests that capillary action, thermal gradients, and convection are primary drivers of evaporation and not vapor diffusion.

Table of Contents

List of Figures

List of Tables

Acknowledgements

Firstly, I would like to thank Dr. Melanie Derby for being my major professor and supervisor throughout my time at Kansas State University. I would also like to thank my committee members: Dr. Betz and Dr. Hansen for their assistance. I would like to thank all who have helped me with the development and experimentation of this project including Benjamin Weinhold, Partha Pratim Chakraborty, and Will VandenBos.

I gratefully acknowledge the support of NSF grant numbers 1828571 and 165141 and the support of the CHIL Lab at Kansas State University. I would also like to thank Kyle Parr and Dr. Kulesza of Texas State University for their help and support.

Dedication

This thesis is dedicated to my parents, John and Allysyn Paap.

Chapter 1 - Introduction

The primary source of water for crops and livestock in the United States Central High Plains is irrigation from the Ogallala Aquifer [1], supplying 30% of the water used in the United States' irrigated agriculture in 2015 [2]. Due to the semi-arid climate of this region, limited rainfall (e.g., 33-74 cm of precipitation [3]) contributes to watering crops, thereby resulting in water scarcity. Reducing the evaporation from soil is one approach to conserving water and improving water use efficiency.

Due to the insufficient rainfall, irrigation from the Ogallala Aquifer is the primary source of water for irrigation on crops and for livestock [4] as well as industry and residential use such as drinking water [1] in western Kansas. This aquifer lies under eight states, with some of the largest portions in Kansas and Nebraska, and provides one-fourth of the total water supply used for agricultural production across the United States [5]. Recent research shows that the aquifer is being depleted faster than it can recharge [6].

The aquifer is vital to the agriculture in this region and the depletion could lead to less agricultural production, which is a large part of the Kansas economy making up 6.8 percent of the total Gross Domestic Product for 2020 with the top exports being beef, wheat and soybeans [7]. The aquifer is also the primary source of water for residents and businesses located in this region as well as the power generation industry. The Holcomb Power Station located near Garden City, Kansas draws the water it consumes from the Ogallala aquifer using six wells [8]. McGuire [9] found that the aquifer has declined by more than 150 feet in parts of western Kansas from 1950 to 2013. To reduce the amount of depletion of the aquifer and benefit agriculture in other semi-arid climates, research is necessary to optimize irrigation and reduce water losses.

A source of water loss occurs when water is irrigated onto crop ground and then evaporated from the soil surface before the crops can utilize it. Surface evaporation is increased when there is little to no plant coverage over an area prior to the plant development in the early growing season [10]. When irrigation occurs, water can become runoff, absorb into the soil and potentially return to the water table, or be lost as water vapor via evaporation or transpiration from plants [11]. The water that is evaporated from the soil surface does not benefit agricultural or environmental uses and can lead to increased water demands since the water has not been absorbed by the plants which are the target of irrigation. Research is being conducted on various ways to prevent water from evaporating from a soil layer [12-16] which, when implemented, would reduce the amount of water evaporated from a soil surface during irrigation.

Chapter 2 - Literature Review

2.1 Introduction

Evaporation from a soil sample requires knowledge of the process of evaporation from porous media, its mechanisms, and what parameters influence these mechanisms. In the next sections, the stages of evaporation from porous media will be identified. Various drivers of evaporation will then be explored followed by parameters that impact these drivers. Finally, the effects of wettability on evaporation will be discussed.

2.2 Evaporation from homogeneous porous media

Evaporation from homogeneous porous media occurs in three stages: the constant-rate, falling-rate, and slow-rate periods [14-19]. The first stage is a nearly constant and relatively high evaporation rate compared to the following stages. This is followed by a falling-rate of evaporation stage where the hydraulic connection of water to the surface breaks down. Lastly, a slow-rate period occurs at relatively lower saturations than the first two stages and is driven by vapor diffusion.

The constant-rate period of evaporation includes water being evaporated from the top surface by convection. The water is supplied to the top surface by capillary action [20] which is the phenomena where fluid rises in thin tubes or throughout porous media, including against gravity [21]. This is due to the attractive interactions between the liquid and the container or porous media and from the liquid molecules interactions with each other causing surface tension. The height of this liquid column within the media is determined by the amount of surface tension relative to gravity. The supply of water to the surface is from the drying front, which is the water level within the soil layer [15]. The constant-rate period is also the region of evaporation described by Jury et al. [22] where the primary driver of evaporation is the thermal gradients of the soil.

Davarzani et al. [23] experimentally determined that changing the surrounding air velocity would impact the evaporation. Increasing the thermal gradients and convection increase the evaporation from the soil layer. Wind temperatures of 22 °C, 30 °C, and 40 °C increased evaporation amounts of approximately 0.5, 0.62, 0.76 kg respectively, after 10 days of experimentation, indicating that increased temperatures of surrounding air led to increased evaporation rates when all other conditions are held the same. Davarzani et al. [23] concluded that the determining factors of evaporation rates for the constant-rate stage are atmospheric conditions and the properties of the porous media. The constant-rate period of evaporation occurs at a nearly constant-rate even as the fluid distribution within the porous media continues to change [16]. As long as capillary forces continue supplying a constant amount of water to the porous media surface, the evaporation rate remains nearly constant.

Saturation is defined as the ratio of the volume of water to the total volume of the void space of a porous media which can range from zero percent for fully dry and 100 percent for fully saturated porous media [24]. Once the soil reaches a low enough saturation that the capillary flow to the surface cannot continue or the capillary flow is broken by another method, the evaporation rate decreases continuously; this region of the saturation curve is called the falling-rate period [25]. This occurs when the drying front, (i.e. the level of water in the porous media) falls to a level within the porous media that the capillaries begin to break. The falling-rate period begins abruptly once the gravitational and viscous resistance overcome the capillary forces of the liquid in the porous media [15].

The final evaporation stage, the slow-rate period, occurs when there is very low saturation of the porous media or when capillary action cannot continue. The slow-rate period can occur for various saturations, but the evaporation rate is considerably lower than the previous stages, for

example, less than one-tenth of that in the constant-rate period [18]. In this stage, the evaporation approaches values near zero and less than five percent of the total water loss occurs in this stage [18]. This stage of evaporation is primarily driven by vapor diffusion which can be derived from Fick's law [14] and is determined by porous media physical characteristics (i.e. porosity, particle size, compaction, etc.) [18].

2.3 Evaporation mechanisms including capillary action and diffusion.

Evaporation from porous media, such as soil, depends on multiple parameters, such as air and porous media temperature, relative humidity, pressure, air velocity, thermal radiation and the physical properties of the media, including pore size, compaction density, and texture of the soil [15, 16, 20, 23, 24]. The importance of thermal gradients within a porous media have been experimentally investigated [22, 26, 27]. In 1957, Philip and de Vries [27] examined the moisture movement in porous media focusing on the thermal vapor diffusion. It was theoretically determined that liquid islands form in porous media that allow liquid movement. A vapor pressure gradient formed due to a temperature field produced a vapor diffusion flux by condensation occurring on one side of the island and evaporation occurring on the other. They determined that the curvatures of the two sides of the island will change until the rate of condensation on one side equals the rate of evaporation on the other. This allows the fluid to flow across the liquid island and accelerate evaporation; the presence of the liquid islands allows a pathway for evaporation in a porous media. This theory led to the development of η, which is the ratio of vapor transfer by the liquid island theory to vapor transfer given by previous vapor diffusion theory that neglected interaction of vapor, liquid, and solid phases and underpredicted experimental results.

Fick's law of diffusion is commonly used as a method to predict the vapor diffusion from soil. This equation gives a method for calculating the diffusion flux from the media that is being evaporated in the slow-rate evaporation stage [14]. The equation is given by:

$$J = \frac{\theta_a^{2.5}}{n} D \frac{C_{sat} - C_\infty}{L_D} \quad (1)$$

$$\theta_a = \frac{V_a}{V} \quad (2)$$

where J is the diffusive flux, θ_a is volumetric air content, V_a is the volume of air within the porous media, V is the volume of the porous media above the drying front depth, n is porosity, D is water-vapor diffusion coefficient, C_{sat} is water-vapor density at the evaporating interface, C_∞ is the water-vapor density at the atmosphere, and L_D is the drying front depth [14]. This equation uses the vapor diffusion coefficient for a porous media with the expression of Moldrup et al. [28] The diffusive flux equation is dependent on the properties of the porous media being investigated.

In 1968, an equation was developed by Cary [26] to predict the fluxes of heat and water from the air space in soil pores using Fick's law of diffusion,

$$J_w = \frac{\beta D p H_v}{R^2 T^3} \frac{dT}{dx} \quad (3)$$

where J_w is the vapor flux of water, D is the diffusion coefficient for water vapor, p is the vapor pressure of water, R is the universal gas constant, T is the temperature, and H_v is the latent heat of vaporization. This allows for the prediction of a steady-state water vapor flux with a given temperature across an air space. For Cary [26], this air space was the small gap between two plates, this correlates to the pore spacing of porous media.

Jury et al. [22] suggested that water vapor movement can be classified as a function of temperature alone; that it is independent of water content for a large range of saturation. Results from multiple evaporation experiments were combined with the theoretical work of Philip and de Vries [27] and Cary [26] to show that Philip and de Vries' theory needed modification to include the ease of vapor transmission across liquid islands due to heat transport variations of liquid and vapor phases. This allowed for the development of the phenomenological coefficient, β, predicted by Cary [26] to calculate the vapor transport and showed the relation of the enhancement factors found by each group.

Lu et al. [29] developed a method for the vapor enhancement factor determined by Philip and de Vries [27], η, by extrapolating soil thermal conductivity to infinite pressure and subtracting the conduction heat transfer from the soil thermal conductivity at atmospheric pressure. The calculated values were compared to the methods of calculating the vapor enhancement factor developed by Cass et al. [30], which used linear regression of the graph of soil thermal conductivity against pressure, and Hiraiwa and Kasubuchi [31], which made assumptions to at low temperatures to approximate the values of soil thermal conductivity to higher temperatures and calculate using atmospheric pressure for specific water content. These results showed that the low temperature approximation of Hiraiwa and Kasubuchi [31] under-estimated the importance of thermal vapor diffusion. The experimental results agreed well with the method developed by Lu et al. [29] and Cass et al. [30] except when the parameters of silt loam were used for calculations of silty clay soil for the method of Cass et al. [30]. This suggests that the soil properties, specifically the structure and texture of the soil, impact the thermal vapor diffusion and that each soil type has a unique vapor enhancement factor.

During the slow-rate period of evaporation, diffusion equations can be very accurate as there are no other forms of water transport in the soil. When the diffusion flux is the driver, it can be calculated using different variations of Fick's law that have been derived to fit the parameters of the problem and account for the liquid island formation within the porous media. These liquid islands enhance the moisture transport within the media which increases the evaporation rate from the porous media. Liquid islands have also been termed "liquid bridges" for their ability to enhance vapor transport. The properties of the media, specifically the porosity, must be known to calculate the diffusion flux [14, 32]. The other primary parameter is the amount of liquid left in the media, as the drying front depth or saturation of the media must be known to make calculations.

Another method of water transport to the surface is due to capillary forces [14-16]. Capillary action depends on the surface energies of the material that will allow the water to adhere to it. In porous media, this allows the water to reach the evaporative surface and maintain constant-rate evaporation [19]. The media acts as if it were a multitude of capillary straws bringing the soil to the surface if the surface tension, pore size, and water amount allow for these connections to occur.

There are many characteristics that are included when determining soil type, including particle size and pore structure, which pertain to soil porosity and void ratio, which are often used to calculate the saturation ratio [24]. Many types of porous media have been examined along with the impacts of particle size. Hellwig [33] experimentally determined that if a water level in a sand layer is kept at the same level below the sand surface, then the evaporation decreases with the coarseness of the sand. For water levels below the sand surface layers, the fine sand investigated had a higher evaporation throughout the trials due to increased capillary action in the sand. However, when the water was kept at the surface of the sand layers, there was no effect on the

evaporation due to the soil composition. The study also compared an open water source to a water level kept at the surface level of the sand and found that the presence of the sand reduced the amount of water evaporated compared to the open source. For non-homogeneous porous media, the percentage of sand present in the soil had an impact on the evaporation rate. An et al. [34] experimentally determined that increasing the amount of sand in a soil mixture extended the length of the constant-rate period of evaporation.

Particle size also impacts the length of the stages of evaporation. If pore sizes are too large in a homogeneous media, capillary action will be very limited [14]. Chakraborty et al. [14] experimentally determined that the first stage of evaporation was insignificant due to the pore size and homogeneous nature of the media being tested (i.e. 0.453mm), the pore sizes were too large to allow the capillary connections and viscous resistance exceeds capillary forces [15]. Smaller pore sizes allow for increased capillary action and increase the length of the constant-rate period of evaporation. A larger pore size disrupts the capillary flow; the increased spacing reduces the amount of water brought to the surface of the media which reduces the surface evaporation losses.

Another parameter that can impact evaporation are wind speeds and air flow above the soil [23]. Once a flow is introduced, fluid dynamic equations must be introduced to predict the evaporation. Davarzani et al [23] used a method of coupling the Navier-Stokes free flow assuming incompressible fluid and Darcy's law for multiphase flow in porous media to develop their model, these equations are the results of the conservation of mass for the liquid and gas phase of water, momentum, and energy balance of the system. The validity of the model developed was investigated experimentally along with studying the variations in evaporation by changing multiple system parameters such as wind temperature, wind speeds, and porosity of the medium. They

determined that increasing the wind speeds increased the length of the constant-rate of evaporation period but has insignificant impacts on the diffusion dominant slow-rate evaporation period.

The degree of saturation is an important parameter in evaporation and the determination of the evaporative stage, it is important to measure the moisture remaining in a media. There are many methods of measuring soil moisture content of porous media, which corresponds to the saturation. Radiation methods, including X-ray, are utilized in field studies [17] and very small scale experiments [14-16]. Dielectric soil moisture probes are also used to measure water content and temperature distribution [23]. Another approach uses the mass loss to measure the evaporation from the soil by measuring mass before and after to calculate evaporation and soil moisture content [15, 16, 34-39]. This can either be done by recording mass of a soil sample throughout the evaporative process to measure the amount lost at each time interval or by taking the mass, drying the sample entirely either naturally or in an oven, and taking the final mass. This method is referred to the measurement of the gravimetric water content [24] or the gravimetric wetness [40].

2.4 Effects of wettability on evaporation

The wettability of a surface is determined by the interaction with the free energies of a liquid, solid, and gas at the solid/liquid interface and the contact line that is formed between them. This relation can be expressed as a form of Young's equation [41]:

$$cos\theta_{CA} = \frac{\gamma_{sv} - \gamma_{sl}}{\gamma_{lv}} \quad \textbf{(4)}$$

where θ_{CA} is contact angle and γ is the interfacial tension where the subscripts *sv*, *sl*, and *lv* denote solid-vapor, solid-liquid, and liquid-vapor, respectively. This equation assumes the surface is smooth and flat, for a porous surface initially entrapped with air and using the contact angle of air and water to be 180^o the equation becomes:

$$cos\theta_{c(CA)} = f_1 cos\theta_1 - f_2$$

(5)

where $cos\theta_{c(CA)}$ is the Cassie contact angle, f_1 is the fractional area of the surface with contact angle θ_1 and f_2 is the fractional area of air-water surface contact [41]. Therefore, the angles of interaction between water and surface provide a measurement to determine whether that surface is hydrophobic or hydrophilic. For a contact angle between the surface and water droplet >90° the surface is classified as hydrophobic. When a water droplet is placed on a hydrophilic surface, the droplet spreads out and has a contact angle <90° [14].

The wettability of a surface can be altered; materials can be coated with chemicals to add a layer of material with a different wettability. Specifically for sand, hydrophobicity is often promoted with a silane solution [42, 43] that adds a nanometer thick, hydrophobic coating to the sand. Water repellency can also occur in nature due to burning of organic matter [44-46]. Fire has been experimentally determined to redistribute and concentrate hydrophobic materials and bond to porous media particles [45]. DeBano [46] concluded that during burning, hydrophobic substance moved downward along temperature gradients, suggesting they are temperature dependent. Robichaud and Hungerford [39] experimentally determined the depth of water repellency was related to the temperature gradient. DeBano [44] determined that, when heated, hydrophobic organic matter can coat adjacent mineral soil particles, thereby increasing water repellency.

It has been experimentally determined that changing the wettability of porous media can have an impact on the evaporation [13-16, 20, 44]. Hydrophobic material can inhibit the evaporation of water by creating a disconnect in the capillary flow [20] or by impeding the capillary liquid flow, which leads to the disconnect in the hydraulic conductivity and the capillary driving force [14]. The water is forced away from the hydrophobic material rather than pulled up to the surface of the porous media. This reduction in capillary action reduces the moisture transport

to the soil surface, like media with very large pore size, and reduces the moisture available to the surface to evaporate.

Single droplet evaporation experiments have been studied comparing the evaporation from a homogeneous simulated soil pore that is created with completely hydrophilic or hydrophobic material. Chakraborty et. al. [12, 13] studied a simulated soil pore using glass (hydrophilic) and Teflon (hydrophobic) beads with a diameter of 2.35 mm at a distance 3.15 mm apart. Using a single droplet of water, they visually measured the evaporation from the soil pore with a camera and recorded the time of total evaporation. Evaporation was compared between the two bead types in an environmental chamber that allowed control of the temperature and relative humidities. The air temperature of 20 °C was used for all trials and relative humidities of 30, 45, 60, and 75 percent were tested with multiple replicates at each relative humidity. For each relative humidity, the water droplet evaporated faster from the glass soil pore than it did from the Teflon pore, indicating the impacts of wettability on evaporation.

Experiments were conducted comparing homogeneous hydrophobic and hydrophilic soil columns. Chakraborty et. al. [14] compared columns of glass and Teflon beads in beakers that were 1.88 cm in diameter and 6 cm in height. These beakers were placed under a 1000 W/m^2 solar simulator at an air temperature of 22.2 °C and 60% relative humidity. Using an X-ray, the drying front depth of the beakers was visualized and compared between material types. The drying front in the Teflon column was approximately 24 mm compared to the glass column which was approximately 30 mm; approximately 25% more water was evaporated from the hydrophilic glass than the hydrophobic Teflon over the same period. In this study, diffusion was the expected driver of evaporation throughout due to the particle size and homogeneous media used.

Altering soil wettability has also been studied by comparing a column of homogeneous hydrophilic soil or simulated soils to various mixtures of wettability. Shokri et. al. [15] studied rectangular columns that were 11 mm by 75 mm with a height of 260 mm in an environmental chamber with a temperature and relative humidity of 25.9 °C and 22%, respectively. These columns of 255-mm-deep samples included a homogeneous hydrophilic column, a hydrophilic column with a 7-mm-thick hydrophobic top layer, a 25-mm-thick hydrophobic top layer, and a 7-mm-thick layer of hydrophobic material buried 18 mm below the hydrophilic surface. By recording the mass of water lost from each column throughout 30 days, the mass loss of water was observed to be 10-20 g for the 25-mm-thick, hydrophobic top layer and 7 mm buried hydrophobic layer, 40 g for the 7-mm-thick hydrophobic top layer, and 50-60 g for the all hydrophilic column. The 25-mm top hydrophobic layer and buried 7 mm thick hydrophobic layer had nearly identical total mass loss. This suggests that the distribution of hydrophobic material is influential to the evaporation.

The results from Shokri et. al. [15] suggest the hydrophilic column drying occurred by capillary induced liquid flow to the evaporating surface until the drying front depth became deep enough to interrupt the hydraulic continuity. The evaporation rate from the 7-mm hydrophobic top layer remained constant as the drying front receded. This was attributed to a constant capillary flow supplied to the hydrophobic/hydrophilic interface, where vapor diffuses through the hydrophobic layer at a constant rate. The 25-mm-thick hydrophobic top layer and the 7-mm buried hydrophobic layer both sustained the drying front at a depth of 25-mm below the surface of the sand, resulting in similar, constant vapor diffusion lengths and reduced evaporation rates compared to the hydrophilic and 7 mm hydrophobic top layer. However, it was suggested that the 7-mm

buried hydrophobic layer did experience evaporation determined to be driven by capillary flow initially from the 18 mm hydrophilic layer above the hydrophobic layer.

Gupta et. al. [20] studied the impacts of varying the thickness of a hydrophobic surface layer above hydrophilic porous media. Beakers 12 cm tall and 8 cm in diameter were filled with 450 g of soil and 190 mL of water were covered with 1 cm, 2 cm, and 3 cm layers of hydrophobic soil. Evaporation reductions of 77.5%, 89.6% and 92.8% were recorded for the 1 cm, 2 cm, and 3 cm layers, respectively, when compared to the uncovered hydrophilic soil. This hydrophobic layer inhibited the capillary flow to the soil surface, thereby reducing the impacts of the surrounding environment and the convective evaporation from the soil surface and reducing the amount of water available at the media surface. The amount of hydrophobic material above the soil also impacts evaporation as the 3-cm-thick layer of hydrophobic material reduced the evaporation more than 1 cm and 2 cm hydrophobic layers. The increased reduction did not form a linear relationship, suggesting that there is an optimal amount of hydrophobic material to place on a surface.

Although soil wettability has been shown to reduce the evaporation, issues may arise from the surface of soil being entirely hydrophobic [45, 47], as hydrophobicity can impede moisture penetration as the outermost layer repels incident water. In an agricultural setting, this can reduce the amount of water available to the plants as the water never reaches the depth of the root system. Debano [44] indicated that surface runoff may carry away important plant nutrients and that treating a water repellent layer with a wetting agent reduces runoff and erosion. When water is irrigated on crop ground, water that does not infiltrate the soil layer can become runoff, thereby potentially causing the leaching of agrichemicals into surface water and groundwater causing contamination [45]. Increased runoff can also mobilize sediment and debris located above a

hydrophobic layer of soil, thereby increasing erosion [48]. Another challenge that can occur is uneven soil wetting [45], which can be undesirable in agricultural production.

Another method of increasing hydrophobic material without increasing runoff was studied by Shokri et. al. [16] which compared mixtures of wettable material, which occur in natural porous media (e.g., soil). Columns of different mixtures of hydrophobic and hydrophilic sand in glass cells 260-mm-tall, 75-mm-wide, and 11-mm-thick were prepared with 0%, 10%, 20%, 50%, and 80% fraction of hydrophobic grains. The more hydrophobic material that is present in the media, the shorter the constant-rate period of evaporation. Each case analyzed with some amount of hydrophobic sand had a shorter constant-rate period of evaporation compared to the uniform hydrophilic sand. The drying front at which the constant-rate period ended was determined to be 130 mm for completely hydrophilic columns, 80 mm for 10% hydrophobic mixture, 62 mm for 20% hydrophobic mixture, and 17 mm for completely hydrophobic column. This indicates that more water remained in the columns with higher amounts of hydrophobic material when the constant-rate period ended. Chakraborty et al. [14] suggest the liquid islands described by Philip and De Vries [27] form 1.5× faster in hydrophilic pores, leading to the creation of the hydraulic connection and increased capillary action compared to hydrophobic pores. The results of Shokri et al. [16] suggest the presence of the hydrophobic material reduces the liquid island formation and disrupts the capillary flow. As the amount of hydrophobic material increases, the liquid island formation and capillary action decrease. The decreased drying rate of the hydrophobic sand was attributed to the lack of hydraulic connection of water to the evaporating surface [16]. The hydrophobic mixtures also all approached near zero evaporation once the constant-rate period of evaporation ended. These mixtures of hydrophobic material would allow water to permeate the

soil layer, reduce the evaporation, and eliminate the impacts of soil runoff that a hydrophobic top layer causes.

2.5 Conclusions from the literature review

Evaporation from porous media is primarily driven by soil properties, soil temperatures, amount of saturation, and the surrounding environment. From homogeneous porous media, evaporation occurs in three stages. The constant-rate first stage is driven by capillary forces pulling the water to the evaporative surface. The falling-rate period of evaporation is where the capillary forces are beginning to break and the drying front depth of the moisture reaches levels too deep for capillary forces to reach the surface. The third, slow-rate stage of evaporation is driven by diffusive vapor flux, which is a much slower transport of moisture than capillary forces.

In previous studies, changing the wettability by increasing hydrophobicity of the soil has been shown to reduce the evaporation from porous media and reduce the length of the constant-rate period of evaporation. Homogenous columns of hydrophobic material had less overall evaporation than hydrophilic columns. Mixing the wettability of materials also reduced evaporation from the material. The evaporation from hydrophilic material is attributed to capillary action bringing the water to the material surface for evaporation by convection. Evaporation in hydrophobic material is driven by diffusion which is a slower form of moisture transport and results in reduced evaporation from material.

2.6 Research Objectives

The research objectives of this study are to investigate the impacts of wettability (i.e., hydrophobicity) on evaporation mechanisms from hydrophilic Ottawa sand to mixtures of hydrophilic and n-Octyltriethoxysilane-coated hydrophobic Ottawa sand. This study will also

scale-up previous research [13-16] with the added component of convection (i.e., constant air flow above and through the sand sample) and inclusion of a solar heat flux.

Chapter 3 - Experimental Apparatus and Procedures

3.1 Experimental Apparatus

To measure the evaporation from porous media at various saturation percentages with continuous air flow and a simulated solar flux, a test section was constructed out of 6.35-mm-thick aluminum plates welded and bolted together with rubber gaskets (McMaster 5812T35) between them for an airtight seal at all connection points. Clear polycarbonate was attached to the side and top of the test section with an industrial adhesive (Loctite AA H8000) that allowed viewing of the sand and a heat flux to be applied on the sand layer from above and provided an airtight seal. Reflective heat tape (McMaster 76035A43) was used on the top of the polycarbonate window to shield the glue from direct heat flux from the solar simulator labeled heat tape in Figure 3-3.

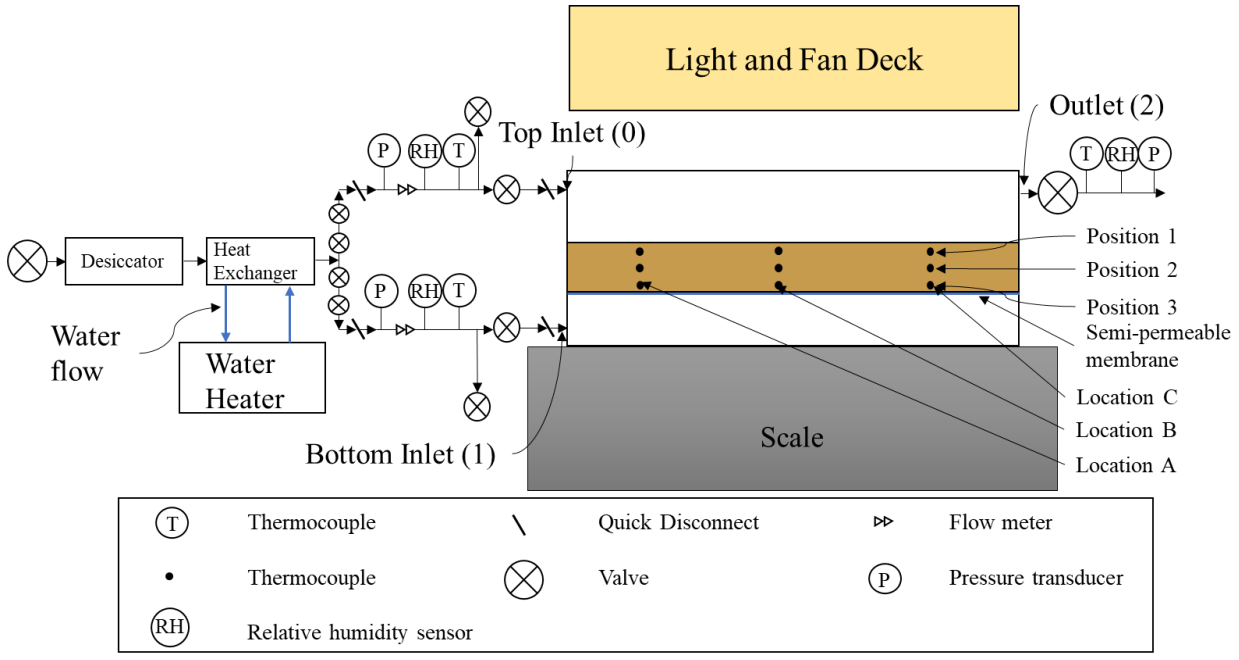

Figure 3-1 Schematic of the experimental apparatus to conduct mass balances on the two inlet flows and single exit flow to determine evaporation rates; dry air enters through inlet 0 and inlet 1, and the air travels above and below/through the sand layer, respectively

To measure the evaporation from a porous media within the test section, constant air flows travelled through the airtight test section and measurements were recorded. Air flowed through holes drilled in each end of the middle section and one end of the bottom section (see Figure 3-2). Holes were drilled in the side of the middle section of the test section for nine thermocouples (Omega TMQSS-062U-6) to measure the temperature of the porous media throughout trials. The thermocouples were placed at locations A, B, and C, 0.079 m, 0.419 m, 0.759 m from the inlet, respectively. The depth below the surface of the sand was at position 1, 2, and 3, 0.008 m, 0.02 m, and 0.035 m, respectively.

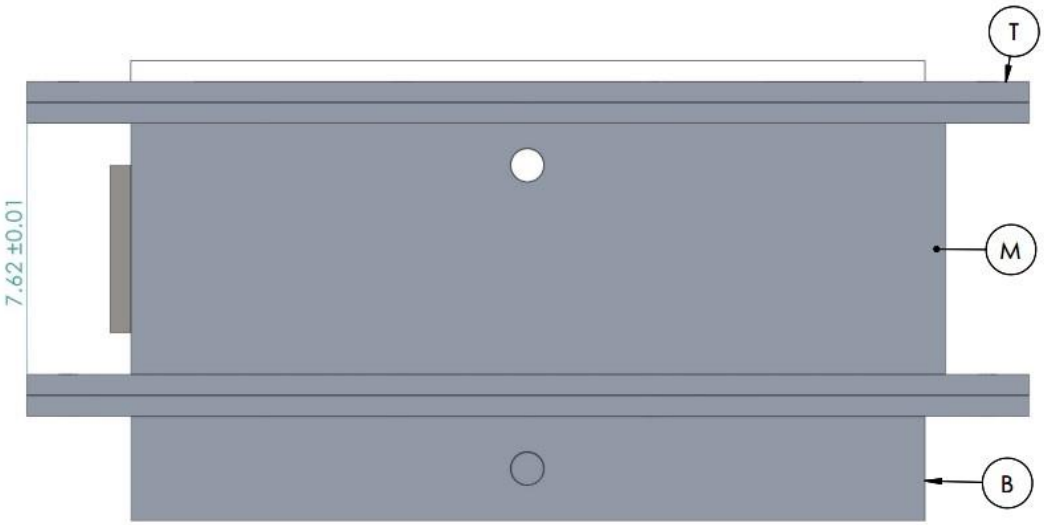

Figure 3-2 Height dimension of the test section in centimeters, inlet ports for air flow are shown, the top, middle, and bottom of the test section are indicated

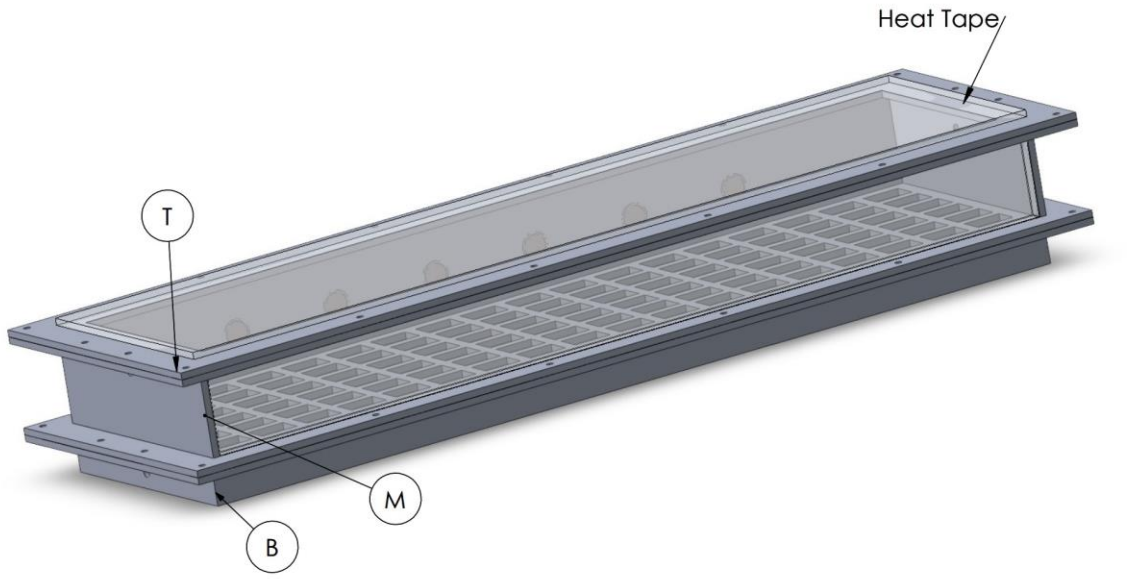

Figure 3-3 Isometric view of the test section showing top, middle, and bottom sections along with metal mesh, the polycarbonate top window is shown and the location of the reflective heat tape is indicated

The air used for the study was building supply air from the Kansas State University Rathbone Hall's air compressors with approximately 827371 Pa (i.e., 120 psi) of supply pressure. The air line was constructed partially of flexible tubing (McMaster DOT Hard Plastic Tubing for Air) to allow for the tubing to be adjusted and removed from the test section for proper mass recordings of the test section. The air travelled through a desiccator (Sharpe 6760 Dryaire Desiccant System) to reduce the supply air to approximately 0% relative humidity. The air travelled through sealed air piping that was submerged in a water bath in the reservoir of a refrigerant chiller (Chiller City RTE-211A) operating as a water bath heat exchanger to heat the dry air within the tubing to the desired operating temperature. The air was brought to a tee junction and split to travel above and below the porous media layer. Swagelok airtight disconnects (SS-QC8-S-810 and SS-QC8-B-810), represented as slash lines on Figure 3-1, were added after the tee

junction and on the air lines just before entering the test section to allow for proper test section mass measurements.

The air flows were controlled by multiple valves (Swagelok Valve SS-45S8) and measurements for pressure and volumetric flow rate were recorded by pressure transducers (Omega PX309-100G5V) and volumetric flow meters (Omega FMA-1609A). The mass flow rate was calculated from the volumetric flow rate measurements by the conversion equation:

$$\dot{m} = \rho \dot{V} \quad \textbf{(6)}$$

where $\dot{m}$ is the mass flow rate of air, ρ is the density of air, and $\dot{V}$ is the volumetric flow rate of air. The volumetric flow rate was taken directly from the sensors while the density was calculated using a function in EES with the variables of temperature, pressure, and relative humidity of the air.

The flows passed through humidity sensors (Omega HX200HR) to measure the relative humidity and over thermocouples (Omega TMQSS-0125U-6) to record the temperature. After these sensors, on/off valves (Swagelok Valve SS-43GM4) were added allowing airflow to travel through the test section or out of the system (see Figure 3-1), this allowed flow to reach operating conditions without entering the test section prior to data collection. After passing through the test section and evaporating water from the porous media, air passed through a Swagelok valve installed to ensure the humidified air was properly mixed and temperature and relative humidity were recorded by Omega thermocouples and humidity sensors.

The humidity sensors and volumetric flow meters produced voltages and current that were recorded in LabView using a data acquisition device (NI cDAQ-9174) that was equipped with a card reader (NI 9207). The thermocouples were connected to the device with a thermocouple card reader (NI 9213). The humidity sensors required power converters to produce the proper current

output (TDK-Lambda LS25-24). The volumetric flow meters were connected to AC to AC power transformers (McMaster 70285K112) to reduce uncertainty from wall outlet sources.

The solar simulator above the test section was constructed using T-Slotted 1”x1” four slotted framing made of silver anodized aluminum (McMaster 47065T101). Seventeen halogen lights (Sylvania 14823) were cooled by five fans (McMaster 1976K63) and were measured using a LICOR light meter and pyranometer (LI-250A and PY106695). The intensity of the lights was controlled by three variable transformers [LVYUAN Variable Transformer Variable Voltage Regulator, 0-130V Output, 110V-120V Input (1000VA) and Staco Energy Model 3PN501B]. The light deck was set to hold the lights above the test section and was bolted to a table constructed of zinc-plated steel channel brackets (McMaster 3310T57). The table uses castor wheels (McMaster 2356T14) to allow for easier movement and includes a layer of rubber between metal connections to reduce energy flow to the table.

During preliminary experiments, large heat fluxes were investigated on the test section at room temperature. This produced condensation on the inner edges of the test section since the aluminum walls of the test section were below the dew point temperature of the inside of the test section, which is approximately 28 C for a 30 C air temperature at 90% RH. To prevent the condensation from forming, a heated blanket was placed around the test section to allow for even heating of the apparatus for proper operating conditions and to also act as a layer of insulation throughout trials (McMaster 3571K31). Fiberglass insulation was affixed on the sides and ends of the test section to reduce the heat energy lost from the system. The entire apparatus was placed on a legal-for-trade scale (McMaster 1852T85) with a capacity of 250 kg that was accurate to ±10 g. The large capacity was required to support the entire apparatus including the sample of water and

sand. The small uncertainty allowed for measurement of the gravimetric water content of the sand and changes in mass throughout experimentation.

3.2 Test Section

The test section, constructed of aluminum plates, was created with three primary welded pieces, a top, bottom, and middle section, which are labeled on Figure 3-2. These three sections were bolted together with a rubber gasket between each of them to ensure proper air tight seal. Inside the test section, the middle section included a metal crossed support (see Figure 3-3) with a single layer of nylon netting (EMD Millipore NY6000010) to hold the sand layer and allow air to pass through. This netting was held into place with duct tape placed along inner side walls of the middle test section. A layer of porous media added to the test section was 5.7 cm deep and was smoothed with plexiglass leveling bars created in house.

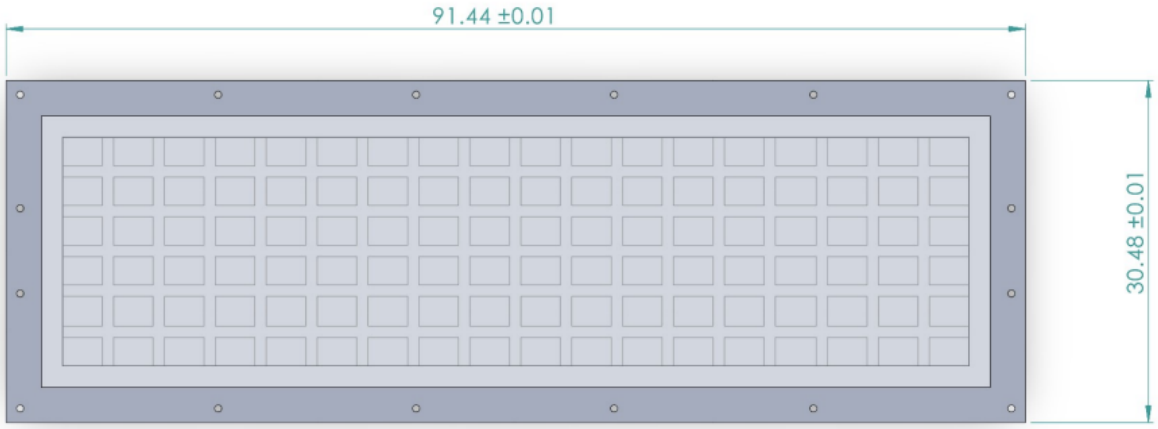

Figure 3-4 Bulk length and width dimensions of the test section in centimeters, metal mesh and bolt holes are shown

3.3 Sand Preparation

The experiments used hydrophilic and hydrophobic 20-30 Ottawa sand (Humboldt Manufacturing Company H-3820BX). This sand was prepared by heating in a convection oven at 105^{o}C for one hour to kill all microorganisms present within the sand. A goniometer (First Ten Angstroms 206140) was used to measure the contact angle of the Ottawa sand. Due to the large particle size and hydrophilic nature of the sand, water applied to the sand was wicked into the soil pores and no water droplet remained to be measured on the goniometer. The Ottawa sand was sieved to a particle size that would not allow the droplet to wick into the pores and formed a surface that would support a droplet for proper contact angle measurement. To view the Ottawa sand, double sided tape was placed on a glass slide and sand placed on the opposite side of the tape. This allowed adjustments of the slide for proper imaging without disturbing the sand layer being analyzed. The measurement of the contact angle of 23 degrees (see Figure 3-4) found using the sieved sand confirmed the hydrophilic nature of the sand.

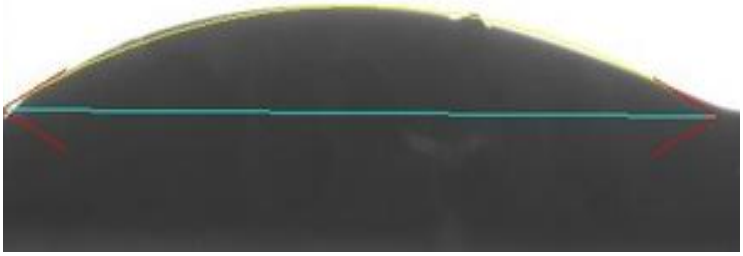

Figure 3-5 Contact angle of an Ottawa sand layer, obtained by Dr. Melanie Derby, contact angle of the droplet is 23 degrees, the blue line represents the water and surface interface

After being heated, the sand was placed in five-gallon containers with lids for clean storage. Sand was placed into the test section completely dry, leveled, and the mass recorded to give an estimate for the amount of sand needed to fill the test section for each experiment. To ensure the

test section was filled and to ensure an excess amount to test for saturation validation, this number was increased by ten percent for each experimental preparation and was measured by mass on the scale into a five-gallon container. Water was then added by mass to the sand to the desired saturation percentage as measured by the gravimetric water content [24]. Challenges arose with this process for hydrophobic sand; water would not penetrate the porous media and more mixing was required than for the hydrophilic sand. This mixture of water and sand was stirred for a minimum of one minute to evenly distribute the water throughout the sand.

The scale was prepared by anchoring all wires to ensure negligible mass alterations would occur from changes outside the test section. The scale was tared so that the amount read from the scale throughout trials was the total amount of sand and water mixture within the test section. The mixture was added in layers that equaled one third of the mass of the initial mixture in the mixing container. Each layer was smoothed to ensure all corners of the test section were filled and minimal air pockets were present. Ottawa sand has been experimentally determined to minimally change in porosity. Bastidas (2016) [49] found porosities ranging from 0.33 to 0.44 using the maximum and minimum dry densities respectively. Kutter et al. [50] used the porosities of 0.369, 0.351, and 0.340 which were calculated from the void ratios of 0.585, 0.542, and 0.515 respectively. The sand density and pore size changes minimally with compression; therefore, change due to compaction was considered negligible. Ottawa sand is entirely silica sand and does swell when water is added; increased amounts of Ottawa sand mixed into an expansive soil were observed to reduce the swelling of the soil [51]. Once the final layer was added, the sand was smoothed with the leveling bar and the excess sand added to a dish to be heated to calculate the saturation of the excess sand and to monitor the saturation of the sand within the test section. The test section was then sealed using a torque wrench (CDI Torque Products 501MRMH) set to 3.389 N·m of torque.

3.4 Sand Hydrophobic Coating Procedure

To alter the wettability of the Ottawa sand, the sand was coated with a silane that created a hydrophobic film on the outside of the sand particles. The procedure used n-octyltriethoxysilane (Fisher Scientific AC338081000) and isopropanol mixed at 10% to 90% by volume respectively based on the procedure from Truong et al. [42]. The chemical reaction occurred by way of a silane adhering to the surface of the sand according to the equation as follows [43]:

$$\equiv Si - OH + C_8H_{17}Si(OC_2H_5)_3 \Longrightarrow \equiv Si - O - Si(OC_2H_5)_2C_8H_{17} + C_2H_5OH$$

Da Re et al. [43] performed an analysis with a scanning electron microscope to compare the surface characteristics (i.e., roughness) before and after the silane coating was applied and determined it to be virtually unchanged.

To begin the coating process, the sand was prepared by rinsing with deionized water three times and dried in an oven at 105 °C for a minimum of 24 hours to ensure the sand was completely dried. The silane and isopropanol were measured in graduated cylinders and combined in glass beakers. Sand was added until a thin film of the solution mixture was still present above the sand. The sand and solution were stirred periodically throughout the 48-hour coating process to ensure all particles were evenly coated.

Once the 48 hours were completed, the sand was removed from the reactive solution and rinsed with deionized water. The rinsing process used a filtration method where deionized water was poured over the sand while it was held in a mesh membrane as well as a rinsing with sand completely submerged in deionized water in a beaker and stirred. Each rinsing process occurred three times to ensure excess silane was properly removed. The silane waste was captured in containers for proper disposal. The sand was dried in an oven at temperatures of 40 °C in glass dishes to maximize the surface area and expedite the drying process. The lower drying temperature

was used to ensure the coating did not deteriorate by exposure to higher temperatures. To ensure proper coating, the contact angle of water on the coated sand was measured using a goniometer to determine if the coated sand was hydrophobic. Figures 3-5 and 3-6 show a water droplet on the silane-coated Ottawa sand adhered to the glass slide with double sided tape. The contact angle on left side of the droplet of 117° and the right side of the droplet of 109°. The coated sand did not need to be sieved prior to the addition of the water droplet as the droplet was not wicked into the pores of the sand but remained on the sand surface.

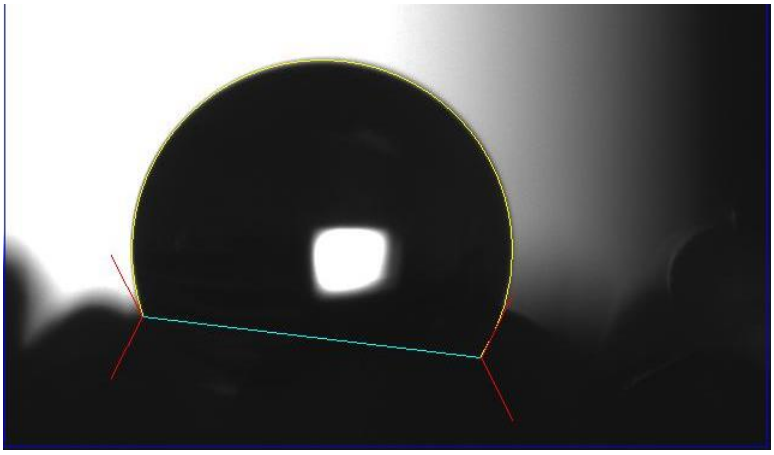

Figure 3-6 The contact angle of silane coated Ottawa sand on the left side of the droplet, the measured contact angle is 117°

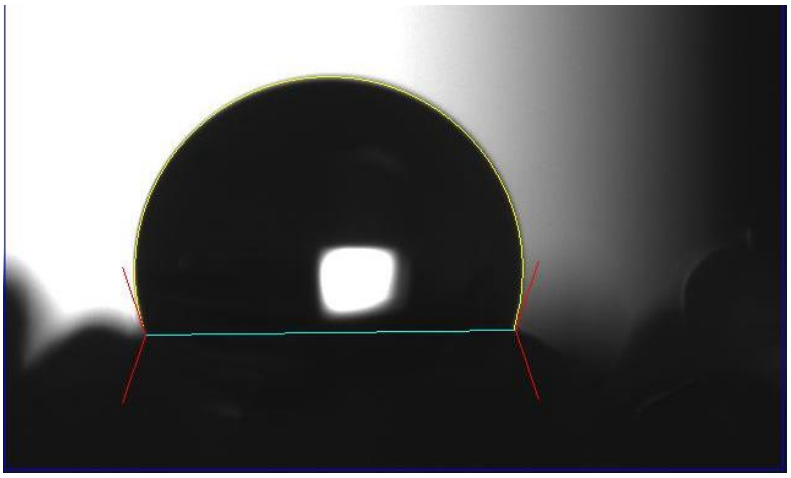

Figure 3-7 The contact angle of silane coated Ottawa sand, the measured contact angle of the right side is 109° and the left side of 117°

3.5 Operating Procedure

To begin, the volumetric flow meters are turned on by switching on the power converters (Power Star and Seven Star Model TC-200). The valves just before the test section inlets (see Figure 3-1) were turned to allow the air flow through the sensors, but to force air out of the system rather than flow through the test section. This allowed temperatures of inlet air to reach operating conditions without impacting the test section. The valves prior to the flow meters were set to prevent pressures from exceeding the capacity of the flow meters. The air was then turned on by operating a valve on the building air supply. The water bath was turned on by filling the reservoir to the proper operating level and the temperature of the bath was set to 65 °C. The air flows were set to approximately 0.0002 kg/s of dry air. The air flowed through the outlets prior to the test section to allow it to heat to the operating temperatures of 27 °C to 31.5 °C.

When the inlet air reached operating temperatures, the top air flow was opened to the test section and the heated blanket was turned on and set to 38 °C. This air flow allowed the test section to heat up without condensation forming on the test section walls. If the test section was heated

without airflow removing the resulting water evaporated from the sand, the humidity in the test section would reach 100% RH. At 100% RH, the source of the evaporation would not be solely from the sand layer. The constant airflow during test section heat-up prevented the humidity from reaching 100% RH. The data were recorded during test section heat-up to ensure the air and test section had reached operating temperatures by measuring the temperatures of the sand layer in LabView. The operating temperature of the test section was set based on the temperature of the sand layer; when all the thermocouples in the sand layer read from 23 °C to 27 °C. Once these operating temperatures were reached, the air lines entering the test section were disconnected by releasing the quick connects (Swagelok SS-QC8-S-810, SS-QC8-B-810), the heated blanket was turned off and the mass of the test section was recorded via the scale.

Once the mass had been recorded, the air lines were reconnected to the test section and lights and fans were switched on. The heated blanket was adjusted so that it did not cover the top of the test section to allow the solar heat flux to be applied to the sand but remained on the scale for proper mass measurement. The inlet flow valves were opened to allow both flows into the test section and the exit valves used to ensure proper operating conditions were closed. The data were recorded in LabVIEW using the DAQ. The solar simulator lights were set to achieve a uniform heat flux across the sand surface as measured by the LICOR light meter and pyranometer. By measuring values throughout the test section, an average solar heat flux was experimentally determined to be 112±20 W/m^2K. Measurements were recorded beneath the polycarbonate top window to ensure the measured heat flux was the applied heat flux to the sand layer.

Trials were recorded for times between 45 minutes and one hour depending upon when the temperature of the outlet flow from the test section reached approximately steady state, determined by the consistency of the outlet temperature recording. Over the hour of data recording, the outlet

temperature graph formed an asymptote that once the outlet temperature approached, was deemed steady state (see Figure 3-8). The results were then transferred to Engineering Equation Solver (EES) and the mass flow rates were calculated using the density of the inlet air with the temperature, pressure, and relative humidity for the inlets and outlet to the test section to convert from volumetric flow rate to mass flow rate.

To calculate the evaporation rate from soil, the temperature, pressure, and RH of the air leaving the test section was used and compared to the air entering the test section using the same parameters. Using the program Engineering Equation Solver (EES), the density of the dry air entering the test section and the mass flow rate of the air was calculated, which was then used to find the humidity ratio, ω, for the flow of air entering and exiting the test section which is the kg_{water}/kg_{air} and was calculated using temperature, pressure, and relative humidity of the air. The change in mass of water within air travelling through the test section was determined by the following mass balance:

$$\frac{\partial m_w}{\partial t} = \dot{m}_0\omega_0 + \dot{m}_1\omega_1 - (\dot{m}_0 + \dot{m}_1)\omega_2 \quad \textbf{(7)}$$

where m_w is the mass of water, t is time, $\dot{m}_0$ denotes the mass flow rate through inlet zero in kg/s, $\dot{m}_1$ denotes the mass flow rate of air through inlet one which is the inlet that travels below and through the porous media, ω_0, ω_1, and ω_2 denote the humidity ratio at the inlet zero, inlet one, and at the outlet, respectively. This equation calculated the change in amount of water in kg between entering and leaving the test section each second; this change is due to the moisture evaporated from the porous media within the test section. The test section was sealed (see section 4.1); therefore, the additional mass flow rate of water must come from the porous media and is the evaporation rate of the test section. The equation was simplified by collecting mass flow rate terms:

$$\dot{m}_w = \dot{m}_0(\omega_0 - \omega_2) + \dot{m}_1(\omega_1 - \omega_2)$$

(8)

where $\dot{m}_w$ is the evaporation rate in kg_{water} per second of the porous media in the test section.

After the trials and EES data processing, the evaporation rates and outlet temperatures were graphed versus time in Microsoft Excel. The outlet temperature graph formed a curve that formed an asymptote that appeared to approach a constant temperature that was deemed steady state (see Figure 3-8). The data were collected from a quasi-steady section of the temperature curve that was formed for the outlet. This steady state was determined from the nearly level portion of the outlet temperature curve shown in Figure 3-8. The quasi-steady temperature was determined by approximating:

$$\frac{dT}{dt} \sim \frac{\Delta T}{\Delta t}$$

(9)

where ΔT is the change in temperature, and Δt is the change in time, which was 500 seconds for these experiments. The values of the slope of the temperature versus time curve were determined to be quasi-steady for all trials when the slope was between 2E-5 and 7.2E-4 K/s corresponding to the temperature changes of 0.01 °C and 0.36 °C over the 500 second period. This was used to find the average evaporation rate over the same time interval of 500 seconds as the steady-state time interval for the outlet temperature.

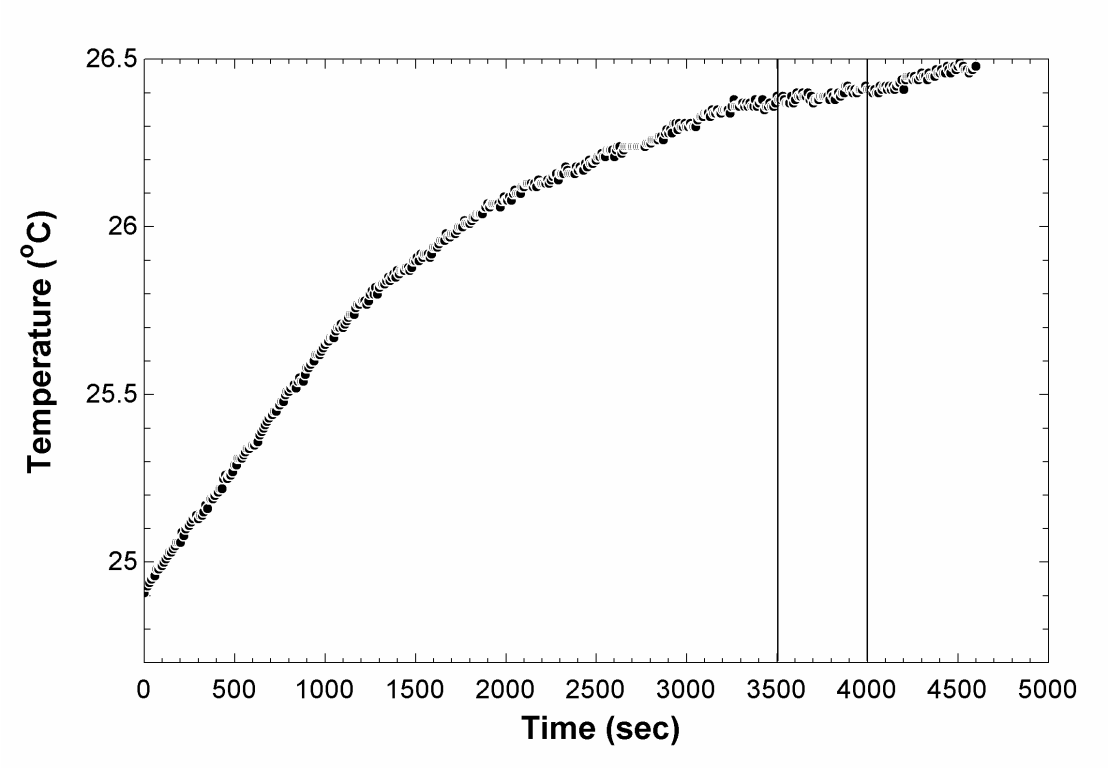

Figure 3-8 Temperature of the outlet throughout the first trial recorded on 2-20-23, average was collected from 3500 to 4000 seconds which is indicated with the vertical lines on the graph

The evaporation rate was graphed against the average saturation percentage of the test section for that trial. The average saturation percentage was measured by recording the mass of the test section before and after the trail and averaging the two values. The average saturation ratio was found using the gravimetric (i.e., mass based) water content of the soil, w [24], in kg_{water}/kg_{soil}. Initially, a mass of sand in measured in a five-gallon container along with an initial mass of water and the container saturation ratio was calculated using the equation:

$$S_{rc} = \frac{w_c G_s}{e} = \frac{\frac{m_{wc}}{m_{sc}} G_s}{e} \quad \textbf{(10)}$$

where S_{rc} is the saturation ratio of the container, w_b is the gravimetric water content of the container, m_{wc} is the mass of water added to the mixing container, m_{sc} is the mass of sand added to the mixing container, G_s is the specific gravity defined as 2.65 for Ottawa soil [49], and e is the void ratio of Ottawa sand. The void ratio for the porous media is dependent on the porosity, n, (i.e., the media pore spacing, 0.35 for Ottawa Sand [52]) and is calculated using the equation [24]:

$$e = \frac{n}{1-n} \tag{11}$$

Once the sand was mixed with water in the container, the scale was tared to zero, the mixture was loaded into the test section, and the mass measurement recorded in the test section was entirely sand and water. The water content of the sand was assumed to remain the same from the container, allowing for the calculation of the mass of sand in the test section:

$$m_{sts} + m_{wits} = m_{in} \tag{12}$$

$$m_{sts}\left(1 + \frac{m_{wits}}{m_{sts}}\right) = m_{in} \tag{13}$$

$$m_{sts} = \frac{m_{in}}{1 + w_c} \tag{14}$$

where m_{sts} is the mass of sand placed into the test section, m_{wits} is the mass of water initially placed into the test section, and m_{in} is the total initial mass placed into the test section. Once placed into the test section, the mass of sand does not change. Therefore, the mass of water for each trial is found by subtracting the mass of sand in the test section from the total mass of the test section for that trial, m_t, allowing for the calculation of the average saturation ratio for that trial:

$$m_{wt} = m_t - m_{sts} \tag{15}$$

$$S_{rt} = \frac{\frac{m_{wt}}{m_{sts}} G_s}{e}$$

(16)

where S_{rt} is the average saturation ratio of the individual trial, m_{wt} is the mass of water in the test section for the trial, and m_{tst} is the mass of the test section for the trial.

3.6 Uncertainty Analysis

Uncertainty in the experimental data collected throughout trials came from sources of uncertainty in data recording and preparation of the samples. The primary uncertainty for the measurements of air flow was due to the uncertainty of the instrumentation used. The upper and lower uncertainty of each device used was determined to be 0.8% of the reading plus 0.2% of the full scale for the volumetric flow meters, 0.2 °C for the thermocouples, 1% RH for the relative humidity sensors, and 0.25% full scale for the pressure transducers.

The uncertainty of the evaporation rate was a combination of the uncertainty in the sensors used to calculate the mass flow rates of air and the humidity ratios used in the calculation of the evaporation rate. This uncertainty was calculated using the following equation from Jeter (2001) [53]:

$$\Omega_{\dot{m}_w} = \sqrt{\left(\frac{\partial \dot{m}_w}{\partial \dot{m}_0} \Omega_{\dot{m}_0}\right)^2 + \left(\frac{\partial \dot{m}_w}{\partial \dot{m}_1} \Omega_{\dot{m}_1}\right)^2 + \left(\frac{\partial \dot{m}_w}{\partial \omega_0} \Omega_{\omega_0}\right)^2 + \left(\frac{\partial \dot{m}_w}{\partial \omega_1} \Omega_{\omega_1}\right)^2 + \left(\frac{\partial \dot{m}_w}{\partial \omega_2} \Omega_{\omega_2}\right)^2}$$

(17)

where $\Omega_{\dot{m}_w}$ is the uncertainty in the mass flow rate of water, $\Omega_{\dot{m}_0}$ is the uncertainty of the mass flow rate of air at inlet 0, $\Omega_{\dot{m}_1}$ is the uncertainty of the mass flow rate of air at inlet 1, Ω_{ω_0} is the uncertainty of the humidity ratio at inlet 0, Ω_{ω_1} is the uncertainty of the humidity ratio at inlet 1, Ω_{ω_2} is the uncertainty of the humidity ratio at the outlet. This shows the sensitivity of an indirect

measurement to a particular direct measurement and the variation from independent origins of uncertainty. The uncertainty for the mass flow rate, $\Omega_{\dot{m}_0}$, was calculated using the same method:

$$\Omega_{\dot{m}_0} = \sqrt{\left(\frac{\partial \dot{m}_0}{\partial \rho_0}\Omega_{\rho_0}\right)^2 + \left(\frac{\partial \dot{m}_0}{\partial \dot{V}_0}\Omega_{\dot{V}_0}\right)^2}$$

(18)

where Ω_{ρ_0} is the uncertainty of the density and $\Omega_{\dot{V}_0}$ is the uncertainty of the volumetric flow rate (±0.8% reading + ±0.2% full scale). The uncertainties of humidity ratio and density are calculated using the maximum uncertainty in the measurements of temperature, pressure, and relative humidity. It was numerically determined that the largest increase in the humidity ratio was due to the upper uncertainty of temperature ($T_{measured}$+0.2°C), the lower uncertainty of pressure ($P_{measured}$-5171 Pa), and the upper uncertainty in the relative humidity percentage ($RH_{measured}$+1% RH). The uncertainty of the density was numerically determined to have the largest increase due to the lower uncertainty of relative humidity, the upper uncertainty of pressure, and the lower uncertainty of temperature. These were calculated using the same EES function used for the initial values, with the uncertainties of the sensors included in the calculation for the uncertainty of density and humidity ratio:

$$\Omega_\omega = \omega_{maximum}(T + \Omega_T, P - \Omega_P, RH + \Omega_{RH}) - \omega_{measured}(T, P, RH)$$

(19)

$$\Omega_\rho = \rho_{maximum}(T - \Omega_T, P + \Omega_P, RH - \Omega_{RH}) - \rho_{measured}(T, P, RH)$$

(20)

where $\omega_{maximum}$ is the maximum value of the humidity ratio using the uncertainty in the measurements of temperature, pressure, and relative humidity; $\omega_{measured}$ is the measured value of the humidity ratio; $\rho_{maximum}$ is the maximum value of density using the uncertainty of the

measurements of temperature, pressure, and relative humidity; and $\rho_{measured}$ is the measured value of the density. The derivatives with respect to each variable were:

$$\frac{\partial \dot{m}_w}{\partial \dot{m}_0} = (\omega_0 - \omega_2) \quad \textbf{(21)}$$

$$\frac{\partial \dot{m}_w}{\partial \dot{m}_1} = (\omega_1 - \omega_2) \quad \textbf{(22)}$$

$$\frac{\partial \dot{m}_w}{\partial \omega_0} = \dot{m}_0 \quad \textbf{(23)}$$

$$\frac{\partial \dot{m}_w}{\partial \omega_1} = \dot{m}_1 \quad \textbf{(24)}$$

$$\frac{\partial \dot{m}_w}{\partial \omega_2} = -\dot{m}_0 - \dot{m}_1 \quad \textbf{(25)}$$

$$\frac{\partial \dot{m}_0}{\partial \rho_0} = \dot{V}_0 \quad \textbf{(26)}$$

$$\frac{\partial \dot{m}_0}{\partial \dot{V}_0} = \rho_0 \quad \textbf{(27)}$$

The value of the initial saturation of the test section was the largest source of uncertainty in the calculation of the average saturation ratio. Previous studies have investigated the uncertainty in partially saturating soils and found saturation uncertainty to be significant sources of uncertainty [54-56]. Li et. al. [54] determined a 3% increase in saturation from the expected value for their

numerical simulation matched the experimental results recorded. Berthoz et. al. [55] calculated stress measurements using a 0%-4% uncertainty in the water content of the sand used.

A target saturation was selected for the experiments and was measured into the mixing container. As the sample was placed into the test section, and overfilled to ensure the test section was entirely filled with sand and water, the sand would not remain evenly distributed with water. The excess sand-water mixture was removed from the test section and the mass of the excess mixture was recorded before and after drying to measure the mass of excess sand and water of the sample. The mass of the excess sand was subtracted from the initial mass of sand in the container to find the potential mass of sand in the test section.

$$m_{sp} = m_{sc} - m_{se} \quad \textbf{(28)}$$

where m_{sp} is the potential mass of sand in the test section, m_{sc} is the mass of sand in the container, and m_{se} is the mass of the excess sand. The same method was used to calculate the potential mass of water in the test section by measuring the amount of water evaporated from the excess sand and subtracting this amount from the amount in the container to find the potential mass of water in the test section.

$$m_{wp} = m_{wc} - m_{we} \quad \textbf{(29)}$$

where m_{wp} is the potential mass of water in the test section, m_{wc} is the mass of water in the container, and m_{we} is the mass of the excess water. The values of the potential mass of sand and water were used to determine the potential water content. The difference between the water content of the container and the potential water content was used for the uncertainty in the water content for a particular experiment:

$$\Omega_{\mathrm{w}} = \left|w_p - w_c\right| = \left|\frac{m_{wp}}{m_{sp}} - \frac{m_{wc}}{m_{sc}}\right| \quad \textbf{(30)}$$

where Ω_{w} is the uncertainty of the water content in the test section, w_p is the potential water content of the test section found subtracting the excess mass of sand and water from the container mass of sand and water, and w_c is the measured water content of the container.

The uncertainty of the average saturation for each trial, $\Omega_{S_{rt}}$, is due to the uncertainty in the measurement of the total mass of sand-water mixture of each trial, Ω_{m_t}, which was the uncertainty of the scale (±10 g), the uncertainty in the initial mass of sand-water mixture placed into the test section, $\Omega_{m_{in}}$, which was the uncertainty of the scale (±10 g), and the uncertainty of the water content in the test section, Ω_w:

$$\Omega_{S_{rt}} = \sqrt{\left(\frac{\partial S_{rt}}{\partial m_t}\Omega_{m_t}\right)^2 + \left(\frac{\partial S_{rt}}{\partial m_{in}}\Omega_{m_{in}}\right)^2 + \left(\frac{\partial S_{rt}}{\partial w}\Omega_w\right)^2} \quad \textbf{(31)}$$

The derivatives of the average saturation ratio with respect to each mass measurement are:

$$\frac{\partial S_{rt}}{\partial m_t} = \frac{(1+w)G_s}{m_{in}e} \quad \textbf{(32)}$$

$$\frac{\partial S_{rt}}{\partial m_{in}} = \frac{-m_t(1+w)G_s}{{m_{in}}^2 e} \quad \textbf{(33)}$$

$$\frac{\partial S_{rt}}{\partial w} = \frac{m_t G_s}{m_{in}e} \quad \textbf{(34)}$$

The uncertainty of the water content for each experiment is calculated in table 3-1. The experiments that included hydrophobic sand included larger value of uncertainty in the water content due to the difficulty of water infiltration, which is an issue that occurs with hydrophobic soils as there is reduced water penetration and increased amount of runoff [45]. The hydrophobic

nature of the coated sand did not allow the water to wick into the pores and even water distribution became more difficult. This was observed when mixing the sand and water in the containers as the water would sit on top of the sand rather than penetrate the layer. After mixing, water was also observed seeping out of the sand layer within the container. The hydrophobic material was difficult to ensure uniform moisture distribution when the mixture of sand and water was added to the test section, leading to higher uncertainty in the water content.

Table 3-1 Calculation of the uncertainty of the gravimetric water content of the test section										
	m_{sc} (g) (mass of sand in container)	m_{wc} (g) (mass of water in container)	w_c (gravimetric water content of container)	Target saturation (%)	m_{se} (g) (mass of excess sand)	m_{we} (g) (mass of excess water)	m_{sp} (g) (potential mass of sand in test section)	m_{wp} (g) (potential mass of water in test section)	w_p (potential gravimetric water content of test section)	$\Omega_w = \lvert w_p - w_c \rvert$
All hydrophilic Ottawa										
	19030	1961.15	0.103	50.72	3570	420	15460	1541	0.0997	0.0033
hydrophobic layer										
Hydrophobic layer	4350	355.97	0.0818	40.27	1640	90	2710	266	0.098	
Hydrophilic layers	19030	1543.64	0.0811	39.92	5610	600	13420	944	0.0703	
Total			0.0811	39.95	7250	690	16130		0.075	0.0061
hydrophobic mixture										
	19030	1568.51	0.0824	40.56	2710	100	16320	1468	0.0899	0.0075

The difficulty in mixing the water into the hydrophobic Ottawa sand led to the largest uncertainty in the calculation of the uncertainty of the average saturation. The term with the uncertainty in water content, Ω_w, was calculated to be much larger than the other two terms, for the trial of 37% saturation for the hydrophilic sand, prior to the square root being taken, the term containing the uncertainty of the mass of the test section for that trial, Ω_{m_t}, was an order of magnitude larger than the other two terms. The largest source of uncertainty in the calculation of the evaporation rate was the uncertainty of the humidity ratio at the outlet to the test section, Ω_{ω_2}. For the trial of 37% saturation for the hydrophilic sand, prior to the square root being taken, the term containing the uncertainty of the mass flow rate of the top inlet, $\Omega_{\dot{m}_0}$, was 5.5E-14 kg^2/s^2;

the term containing the uncertainty of the mass flow rate of the bottom inlet, $\Omega\dot{m}_1$, was 5.3E-14 kg^2/s^2; the term containing the uncertainty of the top humidity ratio, $\Omega\omega_0$, was 3.4E-15 kg^2/s^2; the term containing the uncertainty of the bottom humidity ratio, $\Omega\omega_1$, was 3.5E-15 kg^2/s^2; and the term containing the uncertainty of the outlet humidity ratio, $\Omega\omega_2$, was 2.9E-13 kg^2/s^2.

Chapter 4 - Results and Discussion

4.1 Introduction

Using the test section and methods described in chapter three, evaporation experiments were conducted for three cases: 1) hydrophilic Ottawa sand, 2) 12% hydrophobic layer of hydrophobic Ottawa sand 0.7 cm thick, 1.8 cm below the surface of hydrophilic Ottawa sand, and 3) 12% mixture of hydrophobic sand with hydrophilic Ottawa sand. Chapter four describes the results of the mass flow validation of the test section and the results of the heat flux measurement directed onto the sand layers. The results of each evaporation study are also presented along with temperature profiles and the vapor diffusive flux for each experiment. Discussions of these results and comparisons to previous literature are included.

4.2 Validation Data

To measure the evaporation rate from the test section using the conservation of mass, an airtight seal was required. To verify the test section was properly sealed, flow through the test section was examined by measuring the mass flow into the test section and the mass flow out of the test section. To do so, the test section was sealed with no sand or water inside and connected to the inlet air lines. The inlet flows were recorded in LabVIEW, and the outlet flow was recorded with a rotameter (McMaster 3281K15). The graph of the mass flow rate in and out of the test section is depicted in Figure 4-1a.

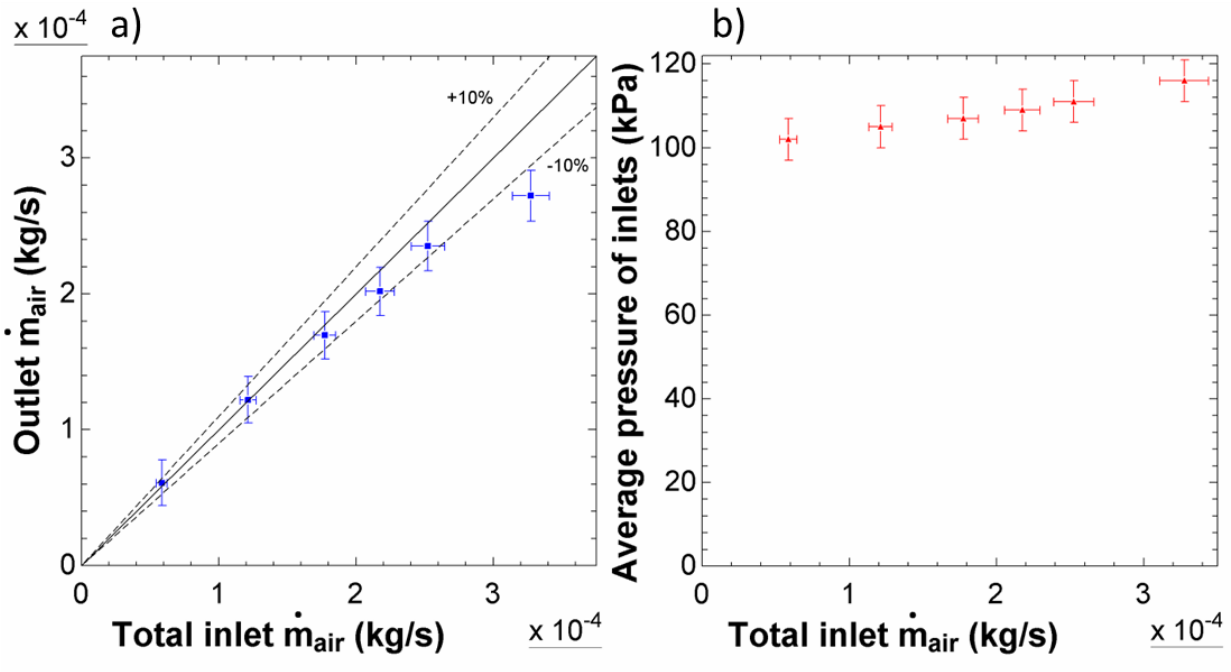

Figure 4-1 Comparison of a) mass flow rate into and out of the test section to ensure proper seal and b) pressures for each mass flow into the test section. Trials run at approximately 0.0004 kg/s with lower pressures of 105 kPa, while validation experiments reached 116 kPa

The mass flow rates were recorded using EES with the same methods of mass flow measurement used for each trial. The outlet mass flow rate was determined with the volumetric flow rate measured through the rotameter. The comparison of the mass flow rate entering and leaving the test section verified the test section was airtight for flows and pressures greater than the flows and pressures used throughout the trials. The flow rates depicted in Figure 4-1a that fall below the one-to-one line are at pressures exceeding that of normal trials, depicted in Figure 4-1b. The increased pressurization was due to the addition of the rotameter. During evaporation trials, pressures for the inlets to the test section were approximately 105 kPa with total inlet air mass flow rates of 0.0004 kg/s while the pressures for the mass flow rate validation reached 116 kPa for the mass flow rate of 0.00033 kg/s. The pressure difference suggests the addition of the rotameter on

the outlet to the test section restricted the air flow and increased the pressure at lower mass flow rates during the validation study.

4.3 Solar flux onto porous media

The solar simulator above the test section was controlled using variable voltage transformers and was measured using a LI-COR pyranometer. The lights were set to the proper radiative flux by varying the supply voltage and measuring multiple points throughout the test section to calculate the average solar flux. The locations of these measurements corresponded to locations of holes initially drilled in the test section for measurement devices that were later sealed with aluminum plugs and industrial adhesive; the locations of the measurements of the heat flux as viewed from above the test section are displayed in Figure 4-2.

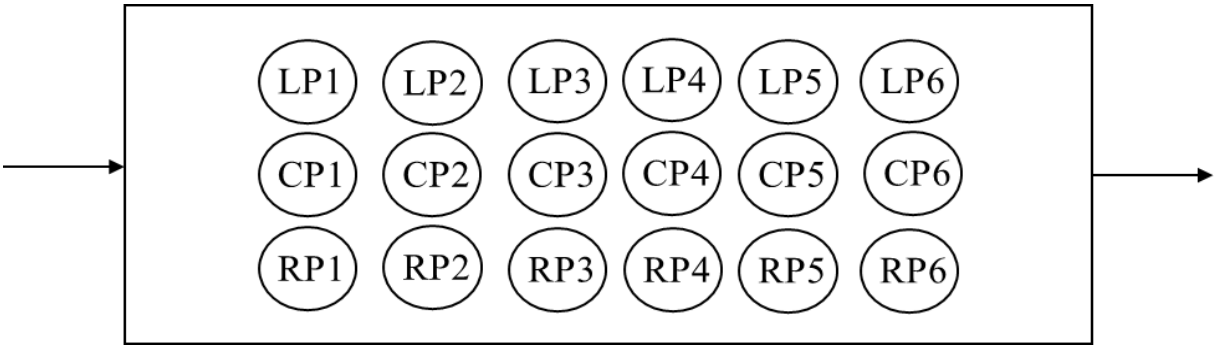

Figure 4-2 Top view of the test section with the locations of recordings listed, inlet and outlet sides of the test section are indicated by arrows

Table 4-1 Measurements of the heat flux applied to the sand layer (W/m^2)

	P1	P2	P3	P4	P5	P6
L	111.06	109.85	107.56	107.44	89.01	93.9
C	117.53	117.8	119.01	121.07	110.51	108
R	113.99	110.2	124.3	132.8	123.3	113.2

These points of measurement were located P1 at 16.51 cm, P2 at 26.67 cm, P3 at 36.83 cm, P4 at 46.99 cm, P5 at 57.15 cm, P6 at 67.31 cm from the inlet of the test section. At each location, measurements were recorded along both side walls [i.e., left (L) and right (R)] and the horizontal center (C) of the test section. The value of the radiative heat flux at each location under the polycarbonate top was measured at the height of the sand within the test section, the value recorded was the solar flux applied to the surface of the Ottawa sand layer being investigated during trials. The average value for all locations within the test section was determined to be 112±20 W/m^2 (two standard deviations).

For each case, experiments were lengthy (e.g., a month). Preliminary experiments without a solar simulator suggested that the falling-rate period of evaporation did not occur until well below 50% saturation. The evaporation rate of the preliminary results is depicted in Figure 4-3. The evaporation for this adiabatic experiment never noticeably dropped regardless of the saturation. No solar heat flux was applied, and no slow-rate period was reached as the evaporation rate remained constant throughout the preliminary experiment.

Using a lower starting saturation was found to be easier to mix and reduced lengthy experimental times. Lower saturations also ensured the water remained in the soil layer. In a preliminary experiment, a sand-water mixture was loaded into the test section with approximately 80% saturated sand; this resulted in water falling through the semi-permeable membrane during packing of the sand. The preliminary results also suggested that there was negligible evaporation from the test section when forced air flows were not run through it. During this preliminary experiment, trials were not run for 10 days, over which the saturation declined from 11% to 10%. The majority of the 1% reduction likely to be due to forced air flow through the test section prior to experimentation on the 10^{th} day. As a result, air was forced through the test section prior to each

trial to reduce the saturation between trials. Trials run on back-to-back days had saturations of 10% and 8% with forced air flows through the test section between these trials.

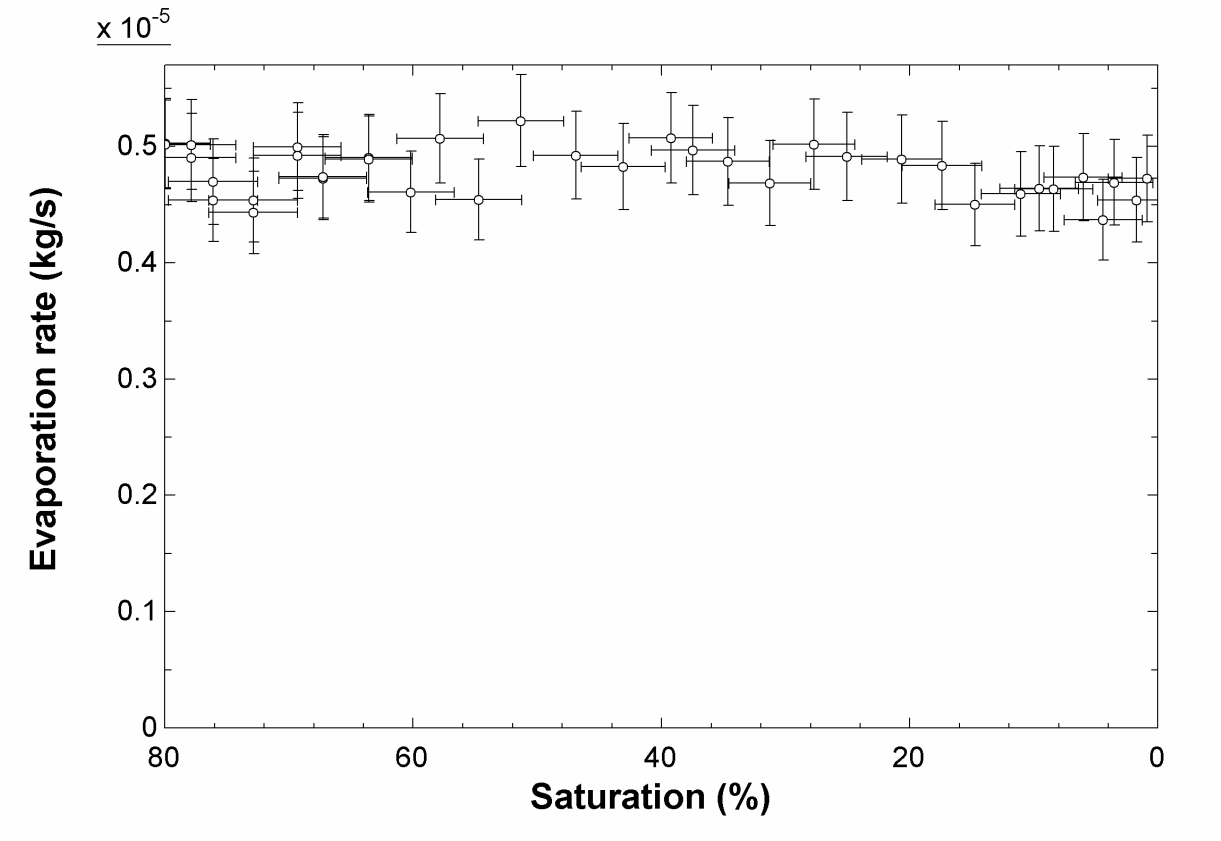

Figure 4-3 Evaporation rate for each saturation for preliminary experiment with no solar heat flux

4.5 Evaporation from hydrophilic Ottawa sand and the effects of heat flux and air flows

Hydrophilic Ottawa sand was added to the test section with a saturation ratio of approximately 50%, but trials did not begin until 37% due to refining the trial procedures and the determination of steady state. For these trials, data were collected until the outlet temperature became quasi-steady for an extended period as shown by a graph developed in LabVIEW (see Figure 3-8). The data were then processed in EES, which calculated the parameters necessary to obtain the evaporation rate from the sand when the temperature was at steady state. A range of 500

seconds was used, and the average evaporation rate was recorded for this range and graphed. The mass of the sand-water mixture in the test section was recorded before and after the trials to get an average saturation percentage for each trial. Evaporation rate vs saturation percentage was graphed to show the stage of evaporation occurring in the test section (constant-rate, falling-rate, or slow-rate evaporation).

The hydrophilic Ottawa sand was entered into the test section by the methods previously described in Section 3.3. Once in the test section and final preparations made, the soil was tested beginning at 37% saturation. The evaporation rate remained nearly constant until noticeably falling around the saturation of 12%. The evaporation rate continued to drop over each trial until reaching a low at approximately 9E-8 kg/s.

Air flow was forced through the test section between trials to reduce the saturation between measurements and to prevent condensation from forming between the trials that would impact the evaporation measurements. Once the saturation stopped decreasing between trials, multiple trials were conducted to ensure the saturation did not decrease further. The amount of water evaporated during and between trials was not enough to alter the saturation percentage and the trial was deemed complete. Figure 4-4 shows the evaporation rate throughout the saturation curve for the hydrophilic Ottawa sand experiment. The collection of a single measurement took 3-4 hours as the test section and air flow were required to reach operating temperatures and the outlet temperature took 45-60 minutes to reach quasi-steady state. The overall evaporative experiment for hydrophilic Ottawa sand took 10 working days to complete.

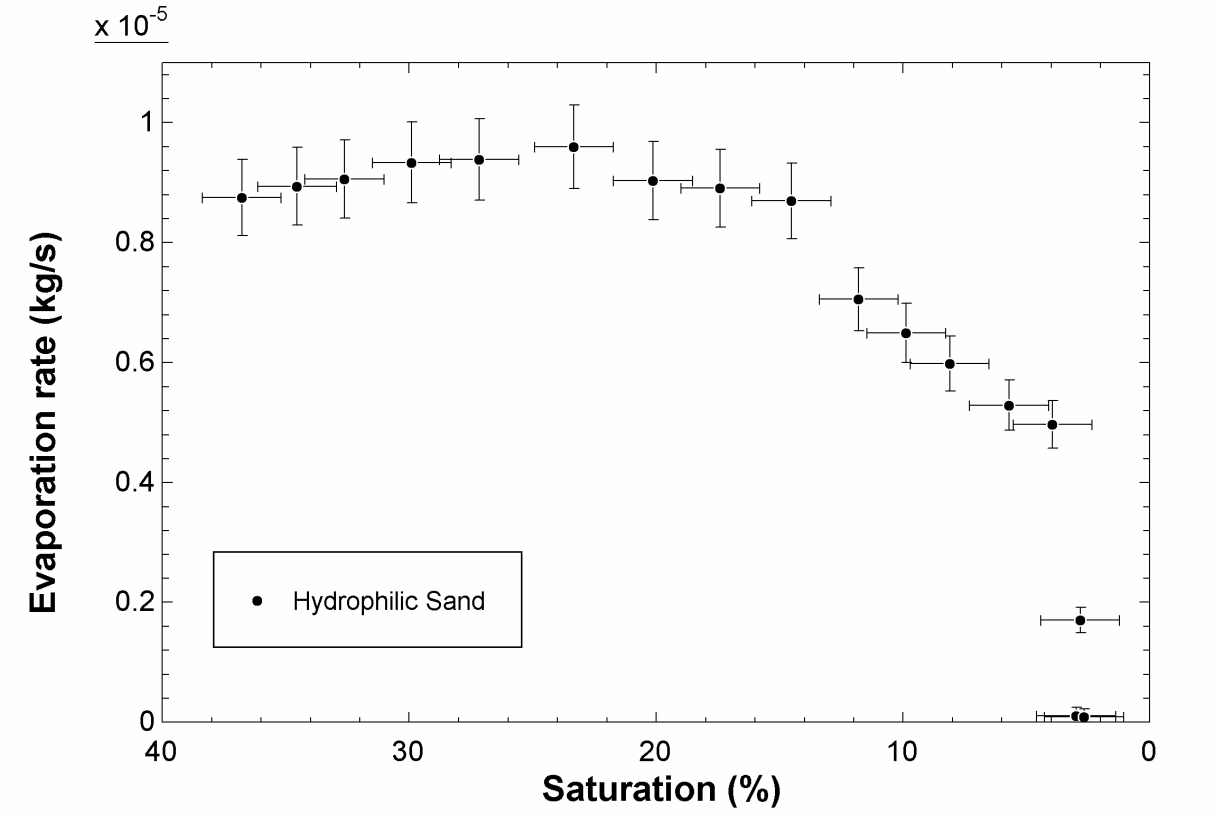

Figure 4-4 Graph of evaporation rate versus the saturation percentage for hydrophilic Ottawa sand

The evaporation rate appears relatively constant in Figure 4-4 from 37% saturation to 15% saturation. This correlates to the constant-rate evaporation described by Shokri et al. [15], as it is relatively high compared to the rest of the experimental points and is also comparatively constant. During this stage, it is hypothesized that capillary action within the Ottawa sand pores brings the moisture to the sand surface for evaporation by convection. The drop in evaporation rate at 12% saturation is the beginning of the falling-rate period, which Chakraborty et al. [14] attributed to the depth of the drying front within the porous media and the loss of the capillary connection of the water to the surface of the Ottawa sand. Shokri et al. [15] describes this as the point where the gravity and viscous resistance overcome the capillary forces. Once the saturation reached

approximately three percent, there was negligible change between trials and there was a negligible amount of evaporation being recorded which suggests the slow-rate period of evaporation has begun that is vapor diffusion controlled.

4.6 Evaporation from a hydrophobic layer of Ottawa sand and the effects of heat flux and air flows

A 0.7 cm layer of silane-coated, hydrophobic Ottawa sand was added to the test section at a depth of 1.8 cm below the surface, which is consistent with experimental design of sand columns in the study conducted by Shokri et. al. [15]. The amount of hydrophobic Ottawa sand was determined to be 12% by weight of the Ottawa sand layer in the test section. This layer was mixed with water to the same level of saturation as the hydrophilic layers above and below it; the target for this experiment was 40% saturation to repeat the starting point of the hydrophilic Ottawa sand experiment. Each layer was added to the test section and leveled with a polycarbonate leveling bar created in house.

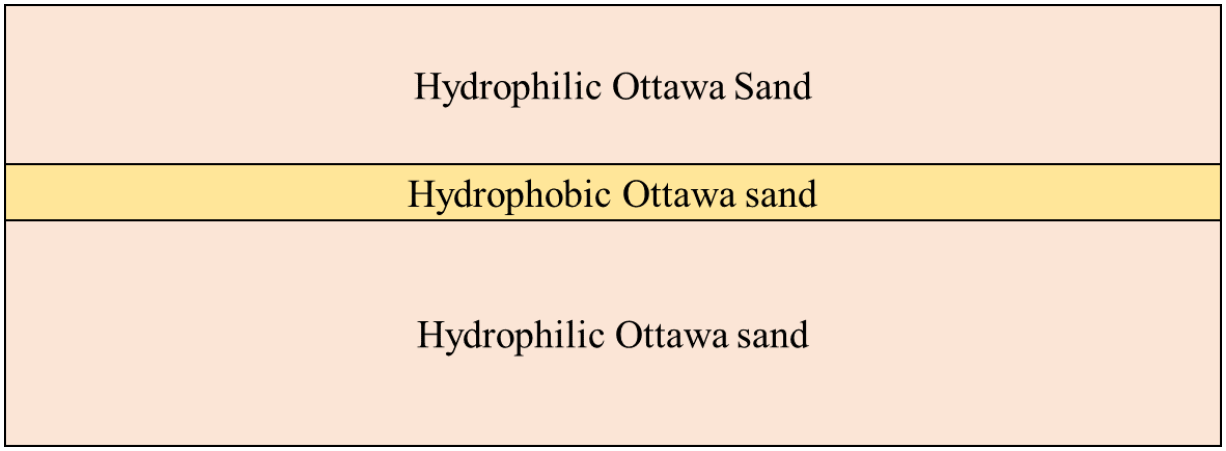

Figure 4-5 Diagram of sand positioning within the test section for the hydrophobic layer experiment

Mixing water with the hydrophobic sand was visibly more difficult than the hydrophilic added to the hydrophilic sand, it was immediately wicked into the layer of sand and only required stirring for equal distribution of the water. The hydrophobic sand repelled the water and stirring

was required to distribute the water equally as well as let the water permeate the sand. Even after stirring, the water would visibly seep out of the hydrophobic sand; constant stirring was required until the sand was added to the test section to maintain uniform moisture distribution. Figure 4-5 displays the evaporation rate over the course of the saturation curve for the hydrophobic layer of Ottawa sand.

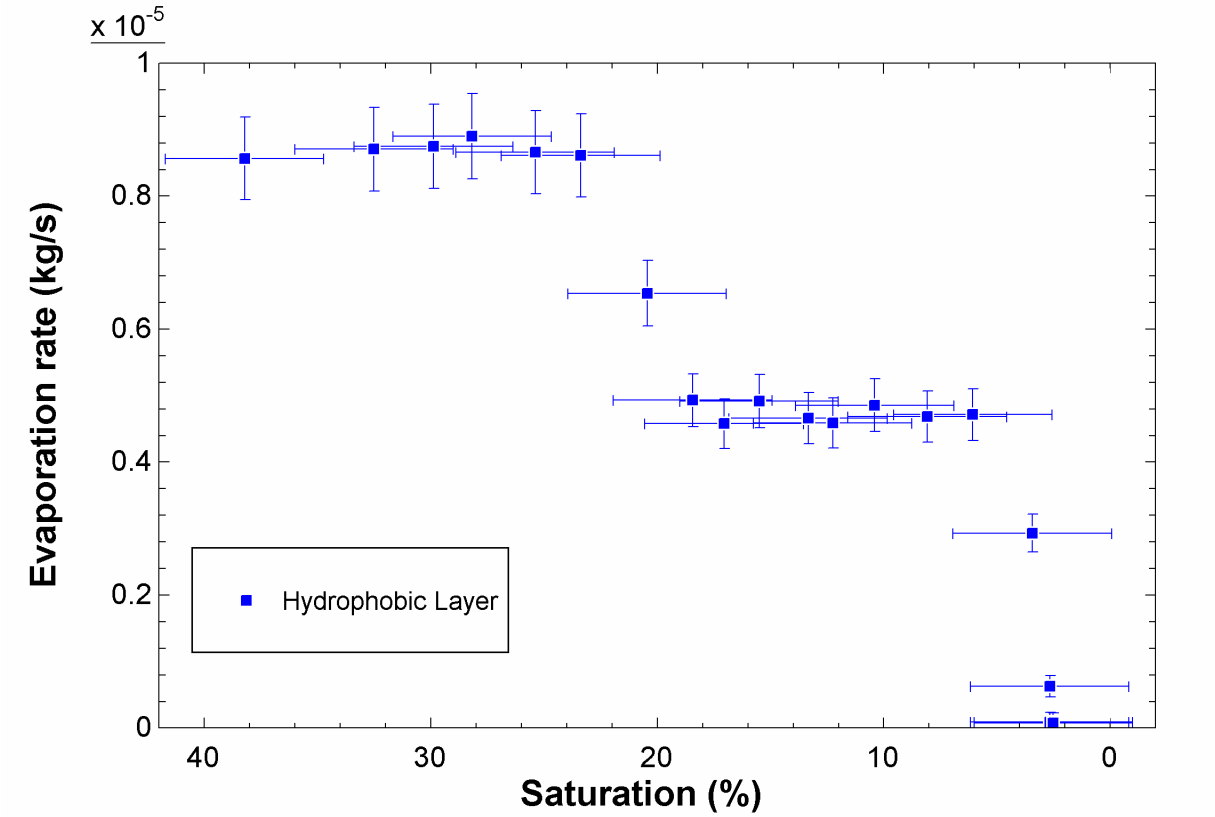

Figure 4-6 Graph of evaporation rate versus the saturation percentage for hydrophobic layer

The data suggest that the evaporation rate drops at approximately 20% saturation and falls to a quasi-steady evaporation rate from 18% to 6% saturation before falling again at 3% saturation. The initial drop in evaporation rate is attributed to the top portion of the sand, the hydrophilic layer above the hydrophobic material, drying out. This is similar to the results of Shokri et al. [15],

where the beaker with a buried layer of hydrophobic material had an initially high evaporation rate, attributed to capillary flow through the hydrophilic material at the surface of the beaker. Once the hydrophilic material was dry, the hydrophobic layer suppressed evaporation by way of interrupting the capillary flow to the surface and reducing the evaporative water loss. The suppressed evaporation in this case is the quasi-steady evaporation from 18% to 6% saturation. The test section has not yet dried out and reached the slow-rate evaporation, but is suppressed compared to the initially high constant-rate period from 38% to 23% saturation. At 20% saturation, there was still sufficient water left to evaporate to prevent from reaching the slow-rate period and complete dry out; however, the layer of hydrophobic material prevented the hydraulic connection to the surface of the soil layer and reduced the overall evaporation.

4.7 Evaporation from a hydrophobic mixture of Ottawa sand and the effects of heat flux and air flows

To maintain a consistent amount of hydrophobic material in the test section for an experiment, a hydrophobic mixture with hydrophilic Ottawa sand was prepared for investigation. Results from experimentation by Shokri et al. [16] suggested that the more hydrophobic material in a sample, the shorter the constant-rate period of evaporation would be. Even the saturation of 10%, the smallest amount tested in that study, had a shortened constant-rate period of evaporation. The 12% mixture investigated here is similar to the 10% mixture used by Shokri et al. [16].

The analysis of the evaporation of the hydrophobic mixture in hydrophilic Ottawa sand is shown in Figure 4-7. The evaporation rate began to fall at approximately 24% saturation and continued to fall gradually until -3% saturation was reached. A negative saturation is likely due to the difficulty in mixing water into the hydrophobic sand and is within the uncertainty in saturation for the hydrophobic mixture experiment. At -3% saturation, the fourth to last trial, the evaporation

became very low, and the saturation changed minimally throughout the remaining three trials, suggesting the slow-rate period had been reached. Shokri et al. [16] determined that as the amount of hydrophobic material increased, the length of the constant-rate period decreased by disrupting the capillary driving forces to the surface.

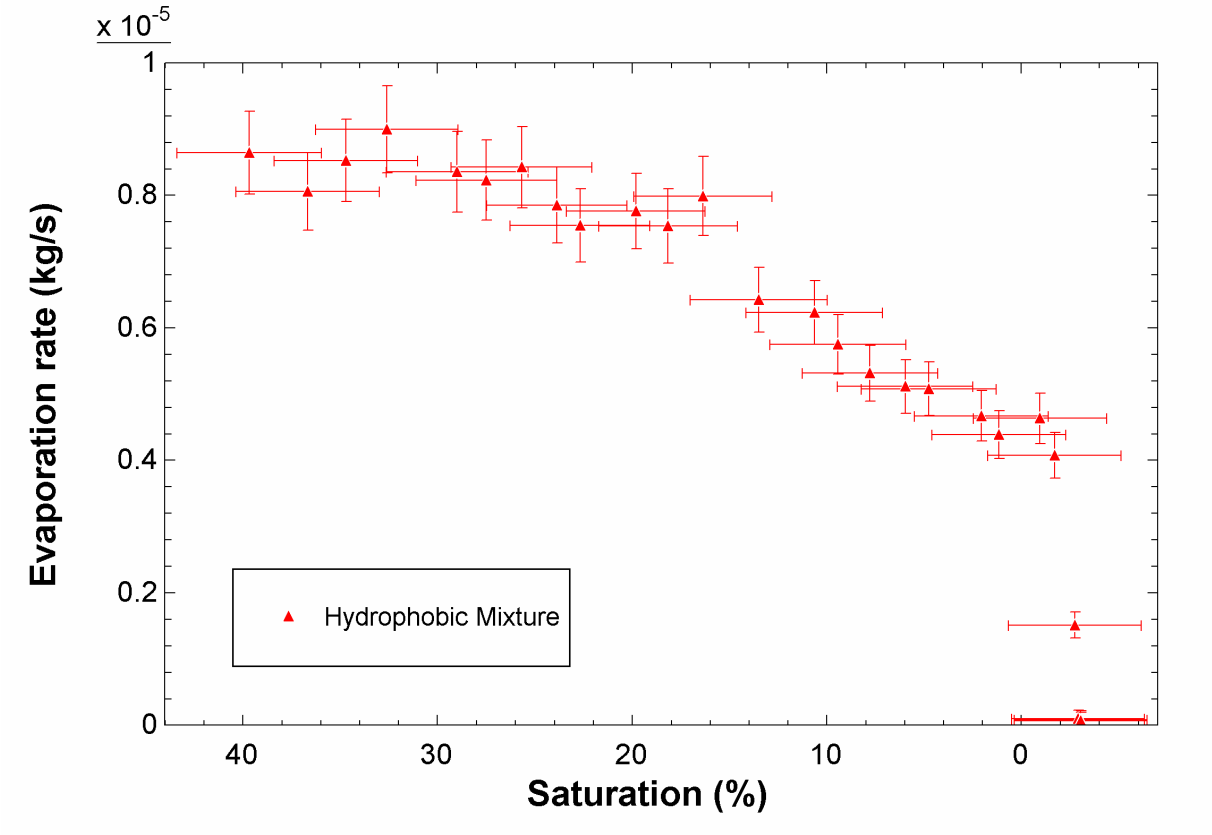

Figure 4-7 Graph of evaporation rate versus the saturation percentage for mixed hydrophobic and hydrophilic Ottawa sand

4.8 Comparison of the three evaporation experiments

The three cases developed were the hydrophilic Ottawa sand test section, a hydrophobic layer, and a hydrophobic mixture in hydrophilic Ottawa sand. The works of Shokri et al. [15, 16] suggests that the three experiments would each have different evaporation rates throughout each

saturation curve and that the longest constant-rate period would occur with the hydrophilic sample. To visualize and compare these experiments, all three were graphed together in Figure 4-8.

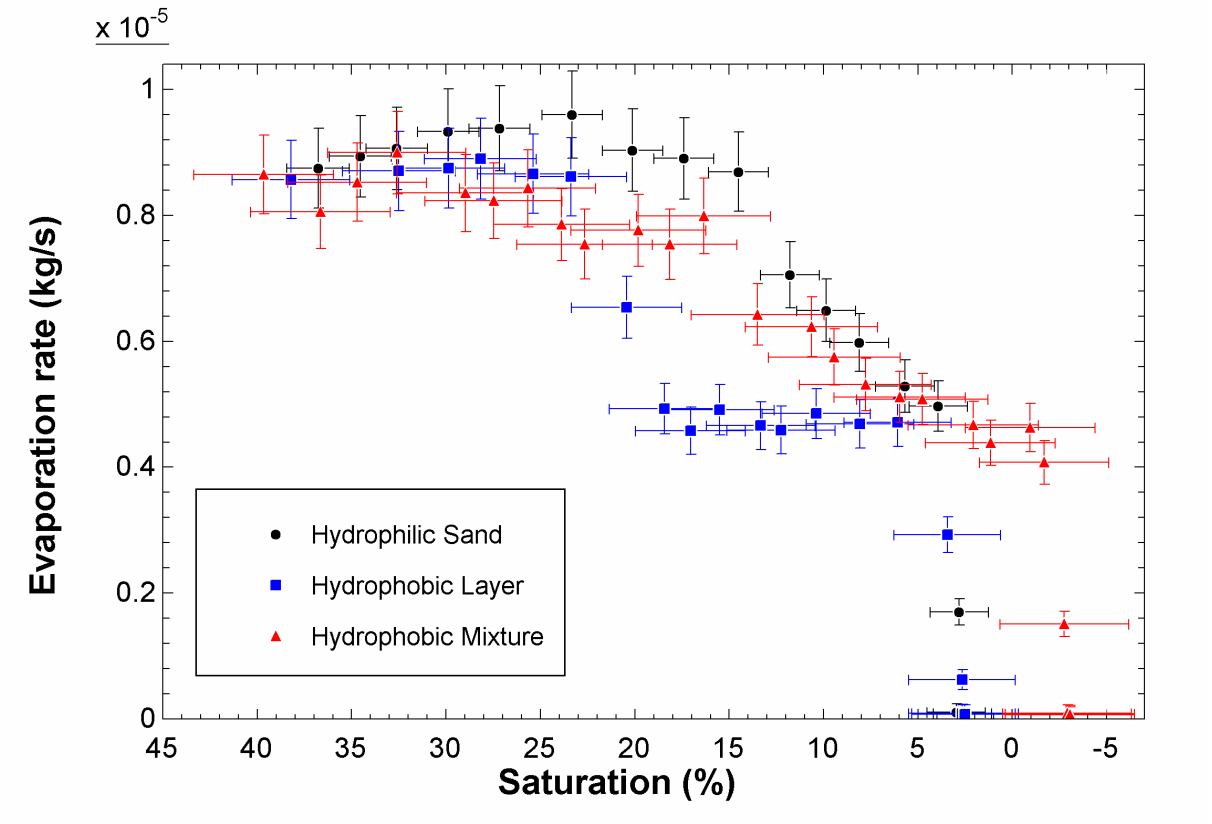

Figure 4-8 Hydrophilic, hydrophobic layer, and hydrophobic mixture experiments graphed for evaporation rate versus saturation percentage

Figure 4-8 shows the hydrophilic experiment remained at the highest evaporation rates for the longest period of saturation, falling at approximately 12% saturation. The hydrophilic Ottawa sand has nothing to impede the capillary action until the saturation becomes so low that the gravitational and viscous resistant forces overcome it, as described by Shokri et al. [15]. Even during the falling-rate period of evaporation, for similar saturation percentages, the evaporation rate of the hydrophilic Ottawa sand is higher than the other two experiments. At approximately 10% saturation, the hydrophilic Ottawa sand experiment had the highest evaporation rate followed by the hydrophobic mixture, and the lowest evaporation rate being the hydrophobic layer. Gupta

et al. [20] described how only water vapor molecules can pass through a hydrophobic channel. The data suggest the introduction of hydrophobic sand in either layer or mixture method can suppress or limit the evaporation at similar saturations.

The shortest constant-rate period was determined to be the hydrophobic mixture which began the falling-rate period of evaporation at the saturation of 24%. This is higher than the hydrophobic layer which dropped at approximately 20% saturation and the hydrophilic sand which dropped at 12%. It was also observed that the hydrophobic mixture had the longest falling-rate period of the three cases, occurring from 24% to approximately -3% saturation.

Another method of discussing the reduction in evaporation is the length of each experiment. Evaporation data were collected for one or two trials each day; however, they were not collected on consecutive days for an entire experiment. Preliminary results (see section 4.4) suggested the saturation dropped minimally over a 10-day-period without forced convection, implying that days between trials would not alter the saturation significantly. Therefore, the trial number was utilized as proxy variable for time as the methods of saturation reduction were the same after each trial. Figures 4-9 and 4-10 display the average saturation and the evaporation rate for each experiment at each trial, respectively.

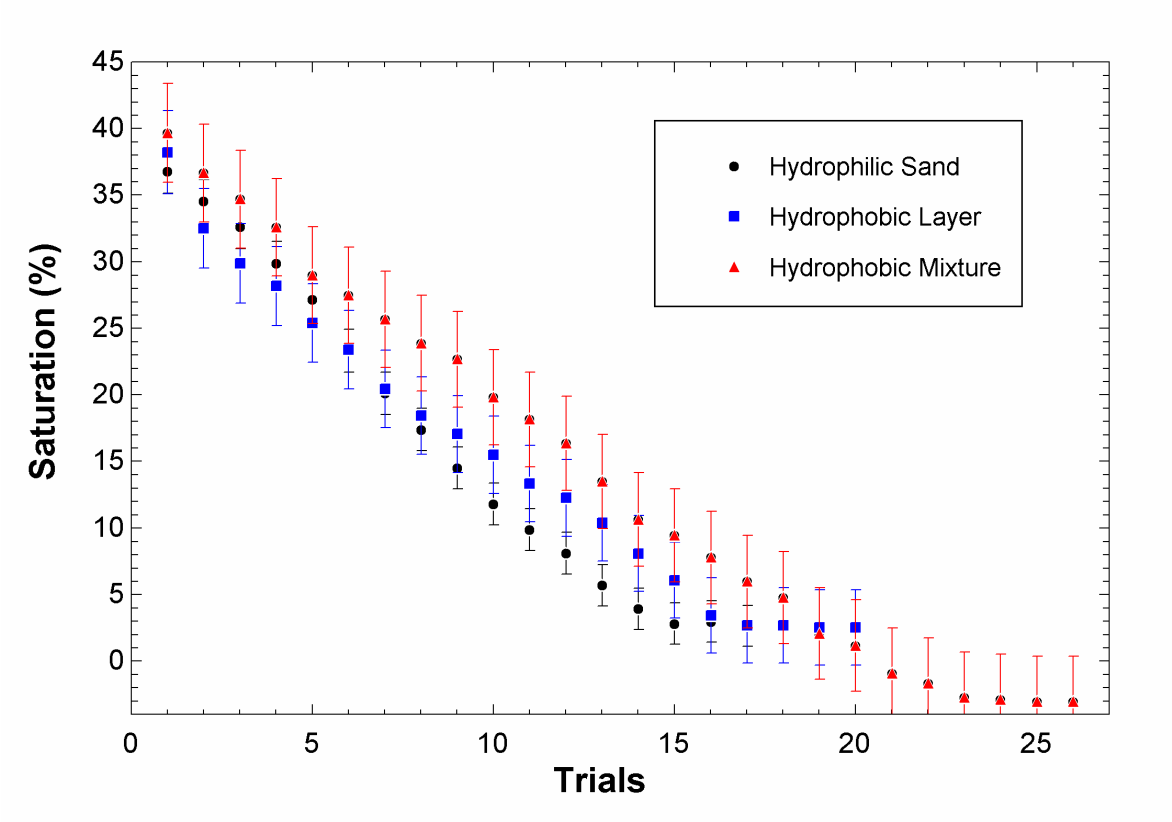

Figure 4-9 Saturation percentage of each trial for each experiment

The hydrophobic mixture took 26 trials to complete compared to 17 trials for the hydrophilic and 20 trials for the hydrophobic layer. Figure 4-9 suggests that the evaporation rate for both hydrophobic experiments was a lower rate than the hydrophilic experiment at a lower number of trials. This means it took a lower number of trials and a shorter period of time to reach lower values of evaporation rate. This can be attributed to the shortest constant-rate period and reaching lower evaporation rates at higher saturations compared to the other two experiments. Reaching lower values of evaporation rate in a shorter amount of time made it difficult to lower the saturation and prolonged the overall experiment. Using the time interval of the first 10 trials, more water had evaporated from the hydrophilic Ottawa sand than either hydrophobic experiment. This implies

that including hydrophobic material into a hydrophilic material will reduce the amount of moisture loss over the same time interval since the evaporation rate has been lowered.

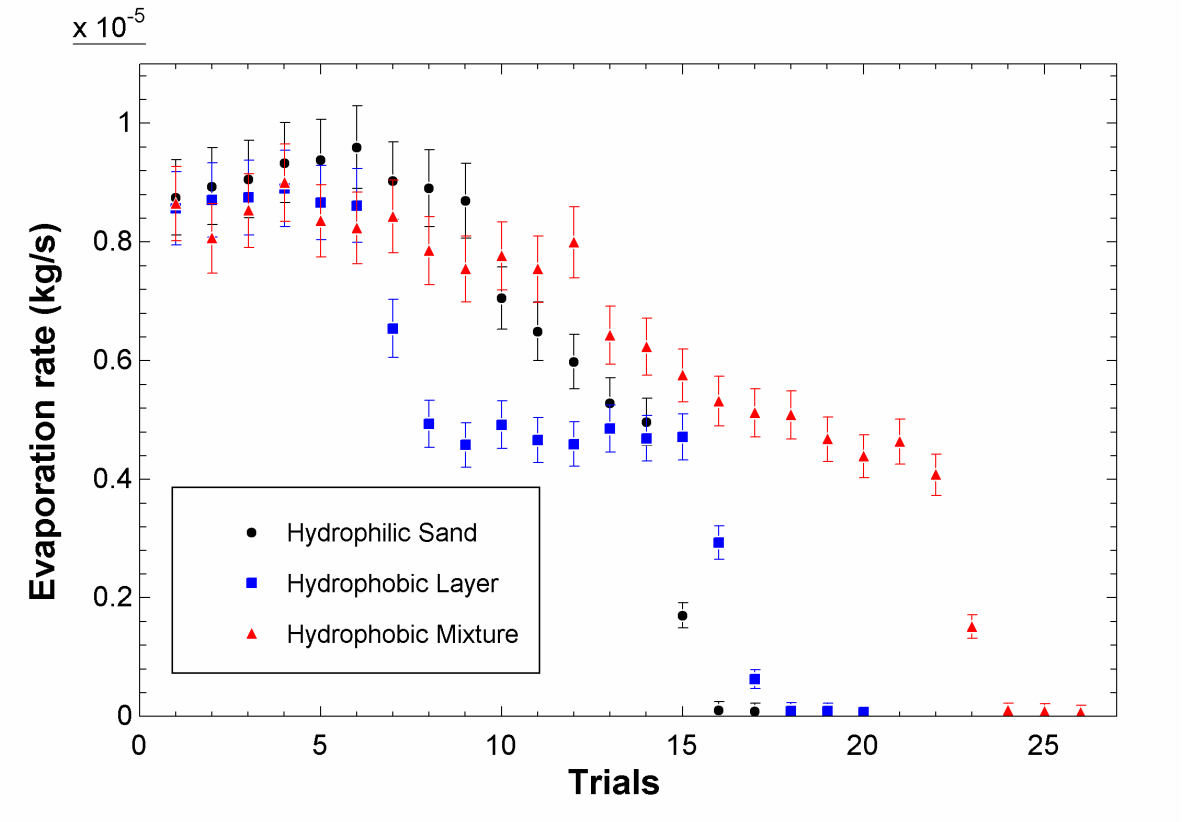

Figure 4-10 Evaporation rates of each trial for each experiment

Each of the three experiments begin the saturation curves at similar evaporation rates. The hydrophobic layer of Ottawa sand begins the falling-rate period of evaporation at a lower saturation compared to the hydrophobic mixture but falls to a lower evaporation rate more rapidly and remains at a lower evaporation rate throughout the rest of the experiment. However, the hydrophobic layer took fewer experimental measurements to complete the experiment. Gupta et al. [20] observed that the uniform barrier of hydrophobic material impeded evaporation more than partial layers. Partial layers still allow some capillary action to the surface whereas a uniform hydrophobic barrier does not. However, this barrier was on the surface in the experiments

conducted by Gupta et al. Shokri et al. [15] also observed the 0.7 cm hydrophobic layer buried 1.8 cm below the surface in a beaker initially had similar evaporation to the hydrophilic beaker before evaporation was suppressed.

The data suggest the buried layer of hydrophobic material was the primary cause of the evaporation reduction because of the constant-rate of evaporation from 18% to 6% saturation after the initial decrease in evaporation rate. Shokri et al. [15] observed nearly constant cumulative mass loss over many days after the initial evaporation had decreased for their 0.7 cm buried hydrophobic layer beaker. This can be attributed to the hydrophilic material below the hydrophobic layer supplying a constant amount of water to the hydrophilic-hydrophobic interface which lead to a constant vapor diffusion through the hydrophobic material. Likewise, the hydrophobic layer experiment maintains a nearly constant evaporation rate from 18% to 6%. This suggests the hydrophilic sand below the hydrophobic layer supplies a constant-rate of water to the hydrophilic-hydrophobic sand interface allowing a constant vapor diffusion through the hydrophobic Ottawa sand. Once gravitational and viscous forces overcome the capillary forces of the bottom layer of hydrophilic Ottawa sand, the evaporation rate is reduced again to the slow-rate evaporation.

Overall, it was observed that the introduction of the hydrophobic sand to the hydrophilic sand layer reduced the constant-rate evaporation period. Although all experiments reached similarly low values of saturation, the experiments with hydrophobic material took more trials to reach the lowest saturation. This suggests that the introduction of hydrophobic porous media to hydrophilic porous media can increase the time to reach 0% saturation and reduce the constant-rate period of evaporation.

4.9 Analysis of temperature gradients within the soil layer

The temperatures near the beginning, center, and end of the test section within the sand layer (i.e., location A, B, and C, respectively) were recorded at locations near the surface of the sand, center of the sand, and near bottom of the sand layer (i.e., position 1, 2, and 3 respectively). The depths of the thermocouples are listed in Table 4-2.

As the sand was heated by the solar heat flux, a temperature gradient formed in the sand layer. The average temperature of each location in the sand was calculated from the same 500 second time interval used for the calculation of the evaporation rate (i.e., the steady state outlet temperature). Figure 4-11, Figure 4-12, and Figure 4-13 show the resulting temperatures for the hydrophilic, hydrophobic layer, and hydrophobic mixture experiments, respectively, at location A, B, and C in the test section for various saturations.

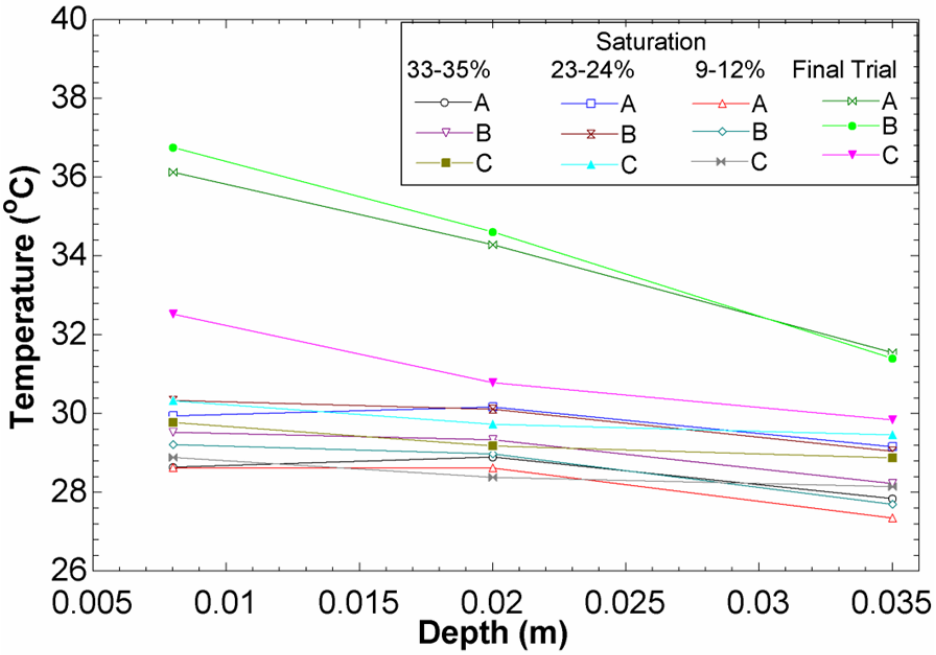

Figure 4-11 Sand temperatures for the hydrophilic sand experiment for a range of saturations

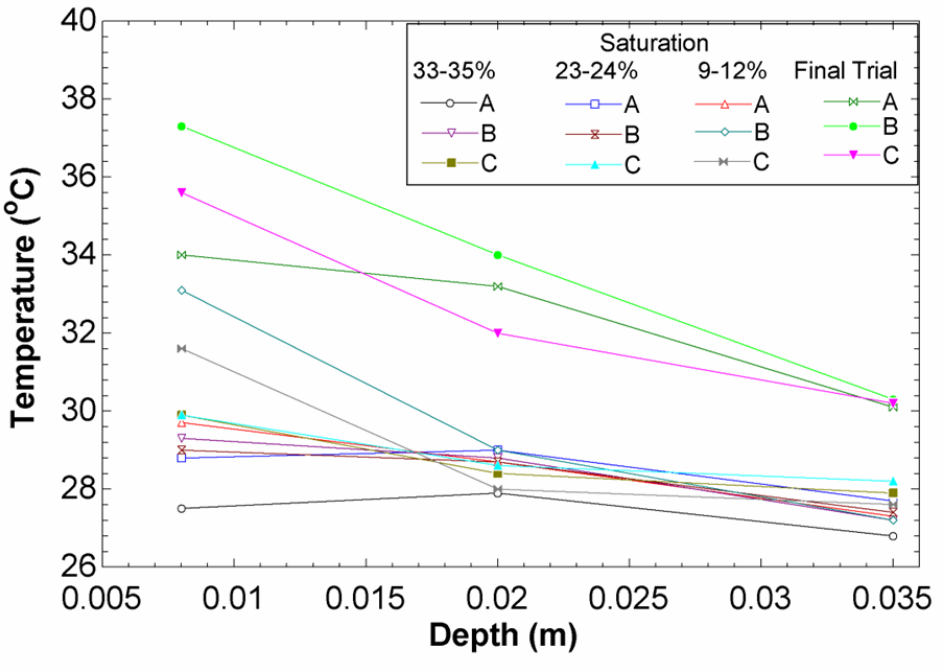

Figure 4-12 Sand temperatures for the hydrophobic layer experiment for a range of saturations

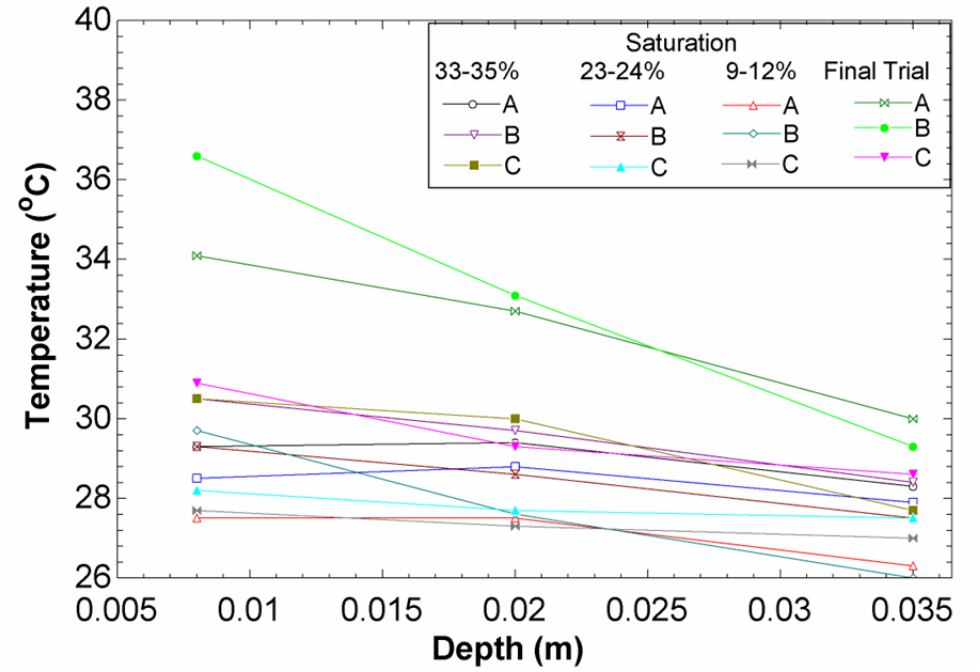

Figure 4-13 Sand temperature for the hydrophobic mixture experiment for a range of saturations

For the higher saturation percentages (i.e., 23-35%) at location A, the thermocouple in position 2 recorded a higher temperature than the thermocouple at position 1, suggesting that there are other forms of heat transfer occurring. A possible source for this difference is evaporative cooling taking place near the inlet to the test section, which would lower the temperature near the surface of the sand but allow a lower depth in the sand to remain a higher temperature. The temperature gradient is not linear, when a linear trendline is added to the graphs of these higher saturations, the R^2 value ranges from 0.57-0.71 for this range of saturations as listed in Table 4-2 for each location in the test section. If the temperature gradient were linear, the heat transfer through the sand would be calculated with Fourier's law [32]:

$$q" = -k\nabla T \quad \textbf{(35)}$$

where $q"$ is the conductive heat transfer flux, k is the thermal conductivity, and ∇T is the temperature gradient.

Table 4-2 R^2 values for a range of saturations at each thermocouple location for hydrophilic Ottawa sand

Saturation	35%	23%	17%	12%	6%	3%
Location A	0.57	0.60	0.71	0.79	0.94	0.99
Location B	0.88	0.90	0.89	0.89	0.95	0.99
Location C	0.95	0.94	0.95	0.94	0.94	0.95

As the sand reaches lower saturations, the temperatures become linear, suggesting there is limited evaporation occurring. The R^2 value is 0.79 for the 12% saturation and is 0.94 and 0.99 for the 6% and 3% saturation respectively, suggesting the temperature gradient in the sand layer is now nearly linear. This can be attributed to the lack of evaporation occurring as there is less water

in the sand. There is limited evaporative cooling occurring, which corresponds to the top surface of the sand increasing in temperature and the temperature profile becoming linear.

The temperature gradients at location B for each experiment were more linear at this location in the test section for the higher saturation values of 23-35%, but position 2 temperature was nearly the same as position one suggesting there is still evaporative cooling taking place. For 33-35% saturation of the hydrophilic trial, depicted in Figure 4-11, the temperature of position one (i.e., closer to the sand's surface) was 29.5 °C while the temperature of position two was 29.3 °C. The R^2 value for the hydrophilic experiment for saturations from 35-12% ranged from 0.88-0.90, shown in Table 4-2. The data suggest that lower saturations (i.e., 3-8%) had linear temperature gradients with R^2 values ranging from 0.95-0.99. This suggests that there is still some evaporative cooling taking place at the surface of the sand for higher saturations, but there is not as much evaporation as there is at the location A thermocouples. A suggested reason for this reduced amount of evaporation is the relative humidity of the air flowing through the test section. The air is dried before entering the test section at approximately 0% RH at the inlet to the test section, and the location A thermocouples are closest to the inlet. The dry air has the most capacity to evaporate water and it is hypothesized that most of the evaporation occurs near the inlet to the test section. As the relative humidity of the air increases, the evaporation potential of the air decreases and less evaporation occurs as the air progresses through the test section.

The temperature profiles of the hydrophilic experiment for location C for each saturation were linear with the R^2 values range from 0.81-0.97 for all saturations, with only one R^2 measurement below 0.93, shown in Table 4-2. This suggests that there is less evaporative cooling and more uniform heating occurring at location C for all saturations studied. It is hypothesized that the humidity of the air at location C is higher than at the inlet to the test section, and air with a

higher relative humidity has a low evaporation potential compared to dry air, therefore there is limited evaporative cooling occurring at this location.

The temperature profiles for the hydrophobic layer experiment and the hydrophobic mixture experiment had similar results. The location A temperature profiles (i.e., closer to the inlet) became more linear as the saturation decreased and location B and C were more linear throughout all saturations. R^2 values for each hydrophobic experiment are listed in Table 4-3 and Table 4-4. The temperature profiles and subsequent R^2 values for the hydrophobic mixture were similar to the hydrophilic experiment. The hydrophobic layer experiment had R^2 values of 0.8 for saturations between 6-17% for location C. A possible explanation for this is the hydrophobic layer restricting capillary flow and causing a non-uniform distribution of the water remaining in the sand layer. This suggests that the hydrophilic layer above the hydrophobic layer became dry while the layer below the hydrophobic sand remained at a higher saturation. A reduced evaporation rate would potentially lead to a lower relative humidity throughout the test section and more evaporation occurring at location C, leading to more evaporative cooling.

Table 4-3 R^2 values for a range of saturations at the locations of the thermocouples for the hydrophobic layer of Ottawa sand

Saturation	33%	23%	17%	10%	6%	3%
Location A	0.45	0.66	0.97	0.99	0.99	0.92
Location B	0.94	0.94	0.92	0.94	0.94	1
Location C	0.92	0.91	0.80	0.80	0.80	0.95

Table 4-4 R^2 values for a range of saturations at the locations of the thermocouples for hydrophobic mixture of Ottawa sand						
Saturation	33%	24%	16%	9%	1%	-3%
Location A	0.71	0.50	0.70	0.76	0.97	0.98
Location B	0.99	0.99	0.99	0.99	0.92	1
Location C	0.96	0.94	0.95	0.95	0.95	0.95

The value of the effective thermal conductivity of Ottawa sand was calculated using the temperatures recorded in the sand layer. The temperature of the airflow through the test section changes minimally, less than 0.5 °C, when the sand was nearly dry (i.e., at the lowest saturation recorded for each experiment), and the convective heat transfer to the air flow is small and assumed to be negligible. This assumption concludes that all of applied solar heat flux is conducted through the sand. To find the effective thermal conductivity of the sand layer, Fourier's law was used. The solar heat flux of 112±20 W/m^2 (two standard deviations) was applied to the surface of the sand layer and the test section was insulated on all sides to prevent horizontal heat transfer. The primary path of heat transfer was vertically downward through the sand layer, therefore, the heat transfer was assumed to be one dimensional [32]:

$$-k_{eff} = q" \frac{\Delta x}{\Delta T} \quad \textbf{(36)}$$

where k_{eff} is the effective thermal conductivity, $q"$ is the conductive heat flux of the sand assumed to be equal to the applied heat flux, Δx is the change in vertical distance through the sand, and ΔT is the change in temperature. This was used to calculate the value of k_{eff} for the final trial of each experiment. Using the conductive heat flux of 112 W/m^2, the distance between position 1 and position 3 thermocouples (i.e., the vertically measured distance between the thermocouple nearest

the surface and farthest from the surface), and the difference in temperature between these thermocouples, the thermal conductivity was estimated for each location for each experiment. The results of this estimation are presented in Table 4-5.

Table 4-5 Effective thermal conductivity values for each thermocouple location in the sand layer and for each experiment (W/mK)

	Location A	Location B	Location C
Hydrophilic	0.674	0.550	1.132
Hydrophobic layer	0.770	0.420	0.563
Hydrophobic mixture	0.740	0.407	1.329

McGraw [57] experimentally determined the thermal conductivity of the dry Ottawa sand to be 0.324 W/mK, with higher values as the saturation increased. At 20% saturation, the value was 0.631 W/mK and at 40% saturation the value was found to be 0.664 W/mK. The estimated values found in Table 4-5 are higher than the value for the dry Ottawa sand determined by McGraw. This suggests that there is still a small amount of water remaining in the test section with more water remaining near the outlet of the test section compared to the inlet and center of the test section, where the data suggest the less evaporation occurred throughout the experimental measurements.

The hydrophobic mixture experimental results were very similar to the results of the hydrophilic Ottawa sand. The hydrophobic layer of Ottawa sand had a lower value for location C, but similar values for location A and B. This suggests that the layer of hydrophobic Ottawa sand induced a more uniform drying of the porous media than the hydrophilic and mixture experiments due to the uniform layer of hydrophobic material. The data suggest that the capillary action in the sand was suppressed by the uniform layer of hydrophobic sand and R^2 values of 0.8 at location C

for 6-17% saturation suggest more evaporation occurring at location C for this saturation range, which could lead to more uniform dry out. The large values of effective thermal conductivity also suggests that an assumption of one-dimensional heat transfer and negligible heat losses to convection and conduction through the sides of the test section may not be valid. Possible sources of heat transfer include horizontal conduction and convection.

Lowering the value of the conductive heat flux would lower the value of the effective thermal conductivity, not all the applied thermal radiation is absorbed and conducted through the sand vertically. Incident radiation can be absorbed, reflected, or transmitted by a surface [58]. The data suggest that some of the incident radiation may be reflected away from the surface, leading to a lower value of the conductive heat flux through the sand. A lower value of the conductive heat flux through the sand would lead to a lower value of thermal conductivity.

Ochsner et al. [17] state that relatively low amounts of water content also increases thermal conductivity of a porous media. They also describe how even a small amount of water in a relatively dry soil can have substantial increase in the thermal conductivity. The water increases the contact between that porous media and has a higher thermal conductivity than air [17], increasing the overall thermal conductivity. The data suggests that small amounts of water may remain in the sand layer at the end of each experiment leading to increased values of thermal conductivity.

Ochsner et al. [17] also describe the impacts of short term weather changes have less impact on the soil as the depth increases and that seasonal temperature variation is more prominent. The surface temperatures depend highly on the temperature of the daily weather cycle and season; however, as the depth of the soil increases, the influence of the daily weather decreases as they are damped out. Soil temperatures measured at a 6-cm depth under vegetation in Minnesota ranged

from 19-37 °C over the course of a single day during the week of measured temperatures. At 1-m depth, the soil temperature ranged from approximately 0-22 °C over the course of a year under vegetation in Minnesota, with temperatures changing approximately 3-5 °C each month. This suggests that the influence of the convection and radiation at the sand surface in these experiments has less impact as the depth in the sand increases. Approximating the heat transfer as one-dimensional conduction does not account for the damped effects of the surface heat transfer as the depth of the sand increases and could lead to different values of calculated thermal conductivity.

4.10 Nondimensional numbers

To compare flows and heat transfer mechanisms across multiple studies, nondimensional numbers can be used. Numbers that are used in heat transfer include the Reynolds number and Nusselt number [58]. The calculation of these numbers can be dependent on the fluid being measured as well as the geometry it is flowing over or through [59], whether it is flow over a flat plate, over a cylindrical tube, or in a duct [58]. As the fluid flows, the velocity near the surface is impacted by the solid object it flows over, creating a velocity boundary layer that changes as it progresses over the surface [59]. For a flat plate, the boundary layer thickness, δ, can be calculated for a position, x, by [58]:

$$\delta = \frac{5.0}{\sqrt{\frac{u_\infty}{\nu x}}} \quad \textbf{(37)}$$

where u_∞ is the bulk fluid velocity and ν is the kinematic viscosity of the fluid (1.6E-5 m^2/s for air at 30 °C). The bulk velocity of the fluid can be found using the mass flow rate of air through inlet 0 for each trial (i.e., 2.0E-4 kg/s) with the equation [58]:

$$u_\infty = \frac{\dot{m}_0}{\rho A_c}$$

(38)

where A_c is the cross-sectional area above the sand within the chamber (i.e., 7.3E-3 m^2). The calculated velocity of 2.3E-2 m/s leads to the boundary layer thickness of 12.1 cm at the length of the chamber (i.e., 83.8 cm) and a thickness of 8.5 cm at half the length of the chamber (i.e., 41.9 cm). Both values of velocity boundary layer thickness are larger than the height above the sand layer within the chamber, meaning a flat plate model cannot be used and the rectangular duct model must be used for nondimensional number calculation.

The Reynolds number is the ratio of the inertial forces to the viscous forces of the fluid [58] and can assist in determining if the fluid flow is laminar (highly ordered flow) or turbulent (irregular with three-dimensional motion). The convection heat transfer depends strongly on whether the fluid flow is laminar or turbulent [58]. For fluid flow in a rectangular duct, the Reynolds number, Re_{D_h}, is calculated by [58]:

$$Re_{D_h} = \frac{\rho u_\infty D_h}{\mu} = \frac{\dot{m}_0 D_h}{\mu A_c}$$

(39)

$$D_h = \frac{4A_c}{P}$$

(40)

where μ is the dynamic viscosity of the air, D_h is the hydraulic diameter of the rectangular duct, and P is the wetted perimeter the fluid is in contact with. The hydraulic diameter was calculated to be 5.6 cm. The average Reynolds number for each experiment was calculated to be 83. The critical Reynolds number (i.e., the value corresponding to the onset of the transition from laminar to turbulent flow) for flow in a duct is approximately 2300 [58], which means the flow through the test section is laminar flow.

The length from the inlet that it takes for the flow to become fully developed, the hydrodynamic entry length, can be approximated for laminar flow using the Reynolds number [58]:

$$x_{fd,h} \approx D_h(0.05Re_{D_h}) \quad \textbf{(41)}$$

where $x_{fd,h}$ is the entry length. For this experiment, the entry length was 23 cm, which is approximately a quarter of the length of the chamber, the flow is approximated to be fully developed for all other calculations.

The Nusselt number, Nu_{D_h}, is a measurement of the ratio of convective heat transfer to conductive heat transfer between the fluid and the surface [58]. The Nusselt number depends on whether the fluid flow is laminar or turbulent, developing, and geometry it flows through or over. For a rectangular geometry, the Nusselt number can be approximated using the ratio of the width and the height of the flow channel, for this study, the ratio is 7.2. Bergman et al. [58] provide a table of Nusselt number values for various geometries with uniform heat flux and uniform surface temperature for fully developed laminar flow in tubes. Extrapolating from this table for the ratio value of 7.2, the Nusselt number is 6.26 and 5.37 for uniform heat flux and uniform surface temperature, respectively. The test section is only heated from the top surface; Bergman et al. [58] and Bejan [59] provide Nusselt values for two flat plates with one side heated by a uniform heat flux and the other side insulated to be 5.39. This is similar to the test section as the solar simulator is applied from above and the sand acts as insulation below. The Nusselt number for the test section is approximated to be between 5.37-6.26, meaning the convective heat transfer occurs 5.37-6.23 times more than the conductive heat transfer.

The values of Reynolds number and Nusselt number were compared to other studies that used forced air flows over porous media. The common practice for field studies is to model the

surface as a flat plate and calculate the flat plate Reynolds number, Re_L,which has a critical Reynolds number for the transition from laminar to turbulent flow of approximately 5.0E5. The comparison of the values of Reynolds and Nusselt number calculated in this study are compared to multiple field studies in Table 4-6.

Table 4-6 Calculated values of Reynolds and Nusselt number for this study and comparison to multiple field studies

Study	**Setting (laboratory or field location)**	**Media**	**Re_L**	**Nu**	**Flow type**	**$\frac{\delta}{L}$**	**L [m]**	**Air Temp (°C)**	**u_∞ (m/s)**
Jacobs et al. [60]	Field study in Spain	Loamy sand with stones	2.0E5 - 8.4E5	560-1690	Laminar to turbulent	0.006 - 0.011	2.7	10-30	0.1-7
Jacobs and Vernhoef [61]	Field study in Niger, West Africa	Loamy sand	1.0E5 - 8.7E5	140-1800	Laminar to turbulent	0.005 - 0.016	6.5	20-33	0.1-4
Gallego-Elvira et al. [62]	Field study in south-eastern Spain	Covered reservoir	4.9E5 - 8.7E5	3360 - 5590	Mixed to turbulent	0.005 - 0.007	45	27-34	0.18-0.32
Calculations from present study using the hydraulic diameter for Reynolds number									
Study	**Setting**	**Media**	**Re_{Dh}**	**Nu**	**Flow type**	**$\frac{\delta}{L}$**	**L [m]**	**Air Temp (°C)**	**u_∞ (m/s)**

Present Study	Laboratory	Ottawa sand	83	5.37-6.26	Laminar	0.019	0.838	27.3-30.9	0.023

These three studies were carried out in areas that were deemed semi-arid climates [60-62], similar to the semi-arid region of the Central High Plains. Jacobs et al. [60] studied flows over a vineyard of bare and pruned grape vine stems in Castilla-La Mancha, Spain, by measuring wind speed and dry and wet bulb temperatures. Jacobs and Vernhoef [61] took measurements in Niger, West Africa, of mean wind speed and mean dry and wet bulb temperatures of fallow savanna. Gallego-Elvira et al. [62] measured the air temperature, relative humidity, and win speed underneath a polyethylene mesh, but above a reservoir located at the University of Cartagena in south-eastern Spain. The air temperatures used in the present study compare well with each of the field studies as shown in Table 4-6; each of the field studies measured temperatures within the range used for the present study. However, the velocity of the field studies is one to two orders of magnitude higher than the velocity of this study.

To perform a scale analysis across the studies, the ratio of the boundary layer thickness to the characteristic length, L, used to calculate the Reynolds number, Re_L. This is done by the equation [58]:

$$\frac{\delta}{L} = \frac{5}{\sqrt{Re_L}} \quad \textbf{(42)}$$

The velocity boundary layer thickness for this study is determined to be half the distance between the top of the test section and the sand layer (i.e., 1.6 cm). Dividing this value by the length of the sand in the test section results in scale values of $\frac{\delta}{L}$ on the same order of magnitude as the field studies.

The Reynolds numbers from each field study are on the order of, or larger than the transitional value of 5.0E5 for flow over a flat plate. Bergman et al. [58] suggest that critical Reynolds number can vary from 10^5 to 3.0E5, this suggests that each of these studies included mixed or transitional flows from laminar to turbulent. The Reynolds number from this study suggests that the flow is only laminar and the critical Reynolds number (2300 for flow in a duct [58]) is two orders of magnitude higher than the value calculated for these experiments.

The Nusselt number values for the field studies are two to three orders of magnitude larger than that of these experiments, which indicate that, in a field, there is a much larger convective component occurring than in this study. A larger Nusselt number indicates more convective heat transfer, compared to conductive heat transfer [59]. The data suggest that in a field, there is more convection occurring relative to conduction than occurs in this study. Keeping all other parameters the same, increasing the mass flow rate of the air through the test section would increase the Reynolds number. The increased mass flow rate could lead to turbulent flows which would increase the convection and the Nusselt number for the flow through the test section [58].

4.11 Analysis of the vapor diffusion flux of water for each experiment

The vapor diffusion flux is the mass transfer of vapor driven by the concentration gradient [58, 59]. This mass transfer is not due to bulk fluid motion, but rather to describe the relative motion of species in a mixture due to the presence of the concentration gradient (i.e., water vapor dispersing into dry air) [58] and is dependent on the temperature and pressure of the fluid and the surroundings. The mass flux of a species, J, can be calculated using Fick's law [58]:

$$J = D_{12}\nabla C \quad \textbf{(43)}$$

where D_{12} is the is the mass diffusivity of component one into component two and ∇C is the concentration gradient. For these experiments, component one is the water within the sand and component two is air. The mass diffusivity is dependent on the mixture temperature, pressure

and composition [59], which can depend on the media the mixture is in. The presence of a porous media can lower the diffusivity of a substance [28] by limiting the volume the substance can disperse to. The vapor diffusive flux of water through the sand layer, J_s, was calculated using Equation 1 [14] and substituting for the drying front depth:

$$J_s = \frac{\theta_a^{2.5}}{n} D \frac{C_{sat} - C_\infty}{L_D} = \frac{\theta_a^{2.5}}{n} D \frac{C_{sat} - C_\infty}{H(1 - S_{rt})} \quad \textbf{(44)}$$

where C is the vapor density, H is the height of the sand layer (5.7 cm for each experiment), and D is the diffusion coefficient of water vapor in air. The diffusion flux is determined by the type of substance undergoing diffusion (i.e., water) and the media (i.e., Ottawa sand) the substance is in, the amount of the substance, the temperature of the media, and the difference in vapor pressures due to temperature and pressure [59].

This equation is used with the following assumptions: 1) the concentration gradient of water in the sand is linear, 2) for completely dry portion of the sand, the volumetric air content is equal to the porosity [14, 15], and 3) the saturation calculated by Chakraborty et al. [14] is the same as the saturation ratio calculated throughout these experiments 4) the diffusion coefficient of water vapor for the temperature of 30 °C (i.e., the average sand temperature for each experiment) was determined to be 2.73E-5 m^2/s [25, 59, 63], sand temperature was used for each calculation. The values of the water-vapor density at the evaporating interface and the water vapor density of the atmosphere (i.e., the air above the sand within the test section) were calculated using the saturated vapor partial pressure and the vapor partial pressure. These are related by the relative humidity of the air above the porous media [64]:

$$RH = \frac{P_w}{P_{ws}} \quad \textbf{(45)}$$

where RH is the relative humidity of the air measured at the top inlet of the test section, P_w is the partial pressure of water vapor, and P_{ws} is the saturated partial pressure of water vapor. The average temperature of the sand was determined to be 30 °C for each experiment which allows for the determination of P_{ws} at the evaporating interface (4246 Pa) [64]. The relative humidity of the top inlet of the test section (i.e., near 0% RH) was used to predict the diffusion fluxes as lower relative humidity results in the largest difference in partial pressures and subsequently the largest difference in the water-vapor densities of the system. This leads to the largest potential value of vapor diffusion flux for the system. Calculations were performed in EES, using P_{ws} and a quality of one to calculate C_{sat}, and P_w and the outlet temperature to calculate C_∞.

To compare the results of the diffusion flux to the evaporative rate from the sand, the evaporation rate was divided by the surface area of the sand layer, 0.19 m^2. This result was the evaporative flux from the sand layer and now has the units of kg/m^2s, the same as the diffusion flux. The diffusion flux of the water vapor and the evaporative flux were both graphed for each saturation for comparison for each experiment, displayed in Figure 4-14.

Figure 4-14 shows the evaporative flux for the three experiments are higher than the diffusion flux until the lowest saturation of each experiment is reached, suggesting that Fick's law under predicts the water transport for this system. Chakraborty et. al. [14] and Shokri et. al. [15] concluded that the slow-rate period of evaporation is controlled by diffusion of water vapor. The data suggest that the evaporation is driven by other methods (i.e., capillary action) until the falling-rate period of the saturation curve ends and the slow-rate period begins. The evaporation flux from each experiment is much larger than the diffusion flux, until the final trials of each experiment, where the experimental values are lower than the estimated diffusion flux. The larger values of the evaporation rate measured are hypothesized to be due to the capillary action, thermal gradients,

and constant air flow present. Philip and de Vries [27] developed their model based on the temperature gradients influencing evaporation and Fick's law underestimating experimental results. They theorized that liquid island formation enhanced vapor diffusion by promoting moisture transport to the surface of porous media, accelerating evaporation compared to the estimation using Fick's law. The experimental design used for these experiments develops thermal gradients in the sand as presented in Section 4.9 that are a potential source of influence in the evaporation flux being larger for nearly the entire experiment.

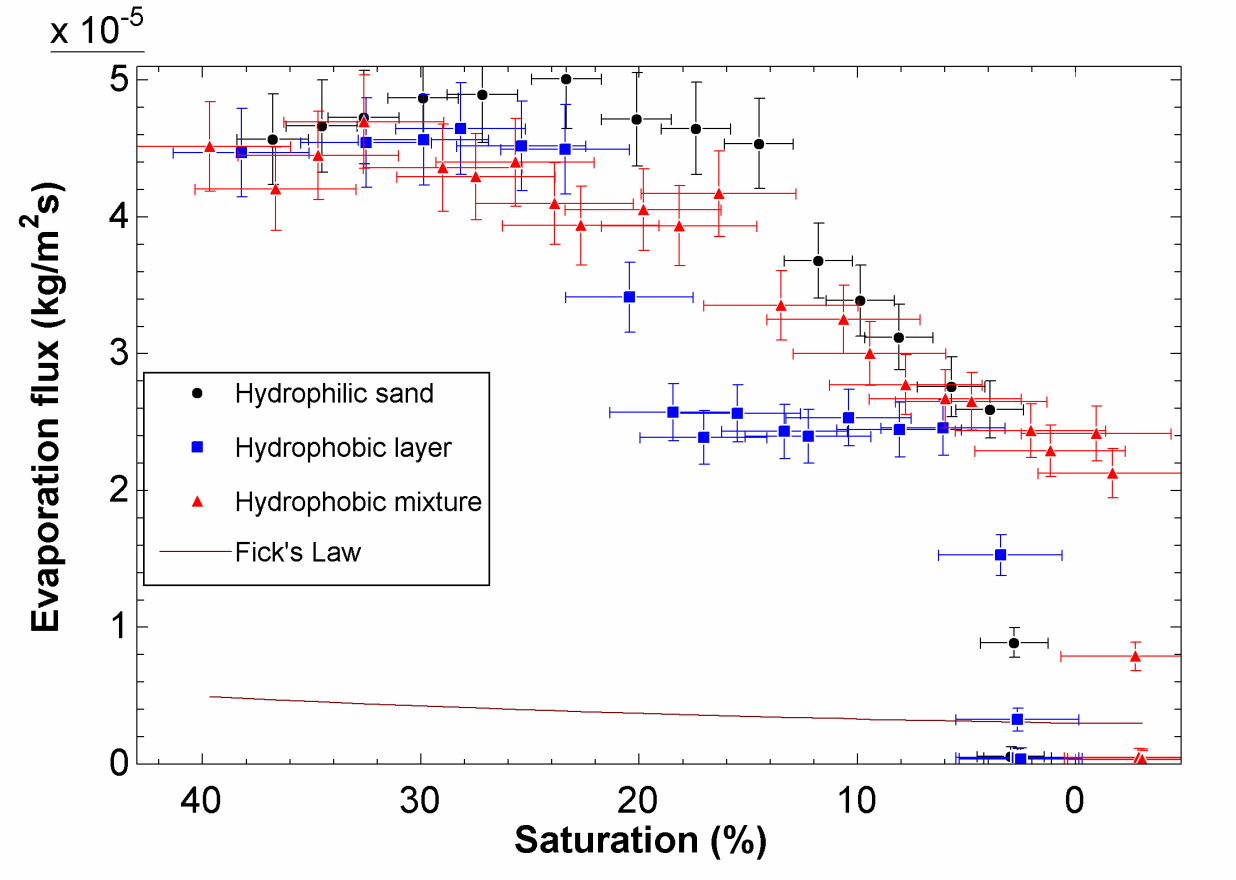

Figure 4-14 Diffusion calculated using Fick's law and measured evaporative flux over the saturation curve for all experiments

Chakraborty et. al. [14] determined that their evaporation rates were initially higher than the rates calculated by Fick's law of vapor diffusion. Although they had a nearly negligible

constant-rate period of evaporation due to the large and homogeneous pore size of their porous media, they still measured higher evaporation rates than diffusion during the falling-rate period. This is consistent with the data presented in Figure 4-14, as the results indicate a constant and falling-rate period with values of evaporation flux up to 12 times higher than the predicted diffusion flux. Philip and de Vries [27] described experimental results of enhanced vapor transport that were 3.6 to 18 times higher compared to simple diffusion predicted by Fick's law. Possible sources of enhanced vapor transport are convective components [23], thermal gradients [26], and liquid island formation [27] promoting more evaporation than simple vapor diffusion alone. The presence of liquid islands increases the hydraulic connection of water to the surface for evaporation in the hydrophilic and hydrophobic experiments but form faster in the hydrophilic pores [14]. In each experiment, these liquid islands enhance the moisture transport from the sand compared to vapor diffusion but form faster and remain longer in the hydrophilic experiment. Both diffusion and the hydraulic connection of water to the top surface increase evaporation compared to diffusion alone [14]. The data depicted in Figure 4-14 suggest a similar enhanced vapor transport occurred in these experiments. The larger values of measured evaporation are expected during the constant and falling-rate periods as capillary action is suggested to be the primary driver of evaporation during the constant-rate period [15]. This suggests that as the capillaries are breaking down during the falling-rate period, there is still increased evaporation compared to the vapor diffusion predicted by Fick's law alone.

The data suggest that as capillary action brings water to the surface of the sand layer of each experiment during the constant-rate period, convection due to the forced air flows increases the evaporation from the sand [23]. Since the air flows and temperatures for each trial in each experiment are the same, the evaporation remains constant until the hydraulic connection begins

to break down [14]. During the falling-rate period of evaporation, possible sources of moisture transport include capillaries that have not yet broken down, liquid island formation and temperature gradients in the sand enhancing vapor diffusion [27], and the air flow through the sand layer from the bottom inlet enhancing vapor transport through the sand layer. These methods of moisture transport would result in higher evaporation flux values than those predicted by Fick's law and are a potential reason for the values of the evaporative flux remaining higher than the estimated diffusion flux until the lowest saturations of each experiment are reached.

Chapter 5 - Conclusions

In this study, three evaporation experiments were performed on Ottawa sand with different wettabilities: 1) a completely hydrophilic layer of natural Ottawa sand, 2) a hydrophobic layer of Ottawa sand consisting of a 0.7 cm layer of coated hydrophobic Ottawa sand 1.8 cm below the surface, and 3) a hydrophobic mixture of hydrophobic sand mixed into hydrophilic Ottawa. The relative humidity, temperature, and pressure entering and leaving the test section were recorded and the evaporation rate leaving the test section was calculated. The gravimetric water content [34] was used to calculate the saturation ratio and the evaporation rate for each saturation was graphed.

Ottawa sand was selected for the low variation in pore size and structure along with being very well studied [49, 50, 65]. Ottawa sand is naturally hydrophilic and a contact angle of 23° was measured with a goniometer. By mixing the sand in a silane solution, the n-Octyltriethoxysilane coated Ottawa sand became hydrophobic with a contact angle of 109-117° as measured on the goniometer. Hydrophobic porous media has been experimentally determined to reduce evaporation compared to hydrophilic porous media [14-16, 19, 20, 41].

Preliminary experimentation revealed the evaporation did not change until low saturations were reached (i.e., <30% saturation); therefore, samples were prepared at approximately 40% saturation for each experiment. The following conclusions about each evaporation experiment, the temperature profiles, and the calculation of Fick's law for each experiment may be drawn:

- The all hydrophilic experiment had the falling-rate stage of evaporation begin at approximately 12% saturation. This experiment took 17 trials to complete. This experiment had the longest constant-rate evaporation and took the least number of trials to complete a saturation curve. Liquid islands have been shown to form the

fastest in hydrophilic pores [14], which increases moisture movement to the surface of the hydrophilic sand, maintaining the constant-rate period of evaporation.

- The hydrophobic layer experiment had the falling-rate begin at approximately 20% saturation. This experiment took 20 trials to complete. This experiment took more trials to complete than the hydrophilic experiment but less than the hydrophobic mixture. The addition of the hydrophobic layer increased water retention compared to the all hydrophilic experiment by reducing the formation of liquid islands. Liquid island formation is suggested to be decreased in the hydrophobic layer, interrupting the hydraulic connection of water to the surface of the sand [15], and beginning the falling-rate period at a higher saturation than the hydrophilic sand.
- The hydrophobic mixed experiment had the falling-rate began at approximately 24% saturation. This experiment took 26 trials to complete which was the most trials to complete and had the shortest constant-rate period of evaporation. Water remained longest in the hydrophobic mixed experiment, and the addition of the hydrophobic material increased water in the sand layer compared to the other two experiments. The data suggest the addition of the hydrophobic mixed reduced liquid island formation throughout the sand layer [14], which prevented the hydraulic connection of moisture to the surface throughout the sand layer, ending the constant-rate period of evaporation the fastest.
- The measured evaporation flux for each experiment was up to 12 times higher than the values calculated for the diffusion flux until the final trials of each experiment, suggesting other forms of moisture transport occur. Suggested methods of increased evaporation flux include capillary action, enhanced vapor diffusion by

way of liquid island formation, and convection due to air flows through the sand layer.

Evaporation from the sand is suggested to be promoted by the formation of liquid islands [27], which promoted the hydraulic connection of water to the surface even as the saturation decreased. Theses liquid islands are more prone to form in the hydrophilic sand than in hydrophobic sand [14]. The hydrophilic sand layer above the hydrophobic Ottawa sand in the hydrophobic layer experiment resulted in a constant-rate of evaporation similar to the hydrophilic experiment as the top surface dried, but the falling-rate of evaporation began sooner than the hydrophilic experiment due to the lack of liquid island formation in the hydrophobic sand pores. The data suggest the hydrophobic mixture had the shortest constant-rate due to the hydrophobic material mixed throughout the entire sand layer, reducing liquid island formation at higher saturations, interrupting the hydraulic connection of water to the surface and starting the falling-rate of evaporation.

The thermal conductivity of the sand at the lowest saturation measured for each experiment was calculated and compared to that of dry Ottawa sand. All values calculated for thermal conductivity were higher than the theoretical value of 0.324 W/m^2K [57]. This suggests that small amounts of water were remaining in the sand and that some amount of incident radiation may be reflected rather than absorbed by the sand [58]. The hydrophobic layer experiment had the lowest value of thermal conductivity near the outlet, suggesting the uniform barrier of hydrophobic material lead to a uniform drying of the porous media. The Reynolds number using a rectangular duct equation and hydraulic diameter was found to be 83 while the Nusselt number for laminar rectangular duct flow was found to be within the range 5.37-6.26 which suggests the flow was laminar and more heat transfer occurred by convection than conduction. However, previous studies

measured in semi-arid climates found Reynolds numbers using the length of a flat plate suggested flows were transitional and turbulent with Nusselt number values were two to three orders of magnitude larger than those of the present study [60-62].

These experimental results suggest that the addition of hydrophobic material to hydrophilic porous media will reduce evaporation rates at higher saturations than hydrophilic media alone. These experiments included both a solar simulator and forced convection above and through the soil. The combination of solar simulator and forced convection components models conditions of a field study more closely than one of these components alone [61]. This research suggests that adding hydrophobic material to a hydrophilic porous media can reduce the duration of the constant-rate of evaporation, maintaining more water in the soil for a longer period of time for plant usage. This is in agreement with the work of Shokri et al. [15, 16] that suggests the depth and amount of hydrophobic material within the hydrophilic porous media can also reduce the evaporation. However, Shokri et al. [16] included a forced convection component on the surface of the columns with an area of 8.3 cm^2, but did not include a solar simulator. The present study included both solar flux and forced convection components to increase evaporative demand over the larger surface area of 1900 cm^2.

The inclusion of hydrophobic material to hydrophilic porous media retained water in the porous media for longer periods of time. In an agricultural field, this would potentially reduce evaporation from the surface of soil, especially when little to no plant coverage is present in the early growing season [10]. Water remaining in the soil longer would provide more time for plants to use the water and require less watering of the plants. Since the Ogallala aquifer provides 30% of the irrigation usage in the U.S. [2], reducing the amount of water lost from the soil surface and increasing water availability to plants would reduce the irrigation needs. The reduction of the

irrigation demand from the aquifer can reduce water demand and potentially reduce the depletion of the aquifer that has been recently observed [6, 9].

Future research possibilities include varying the depth of the hydrophobic layer and altering the amount of hydrophobic material in the mixed hydrophilic and hydrophobic experiments. When compared to field studies, the laminar flow and relatively low value of the Nusselt number suggest that increased mass flow rates of air should be used to model field studies. It would be interesting to investigate a completely hydrophobic test section, as well as other methods of altering soil wettability. Guitierrez et al. [19] determined that soil wettability can be altered by including a bacteria (*Bacillus subtilis*) or a surfactant (Surfactin) and impacted the evaporation using 12.5 g containers of soil.

Introducing hydrophobic material in a field setting would also be a future possibility for experimentation. Previous research suggests that the hydrophobic material applied to a field should be mixed into the soil, rather than a layer applied to the surface, to prevent runoff, which can be damaging to fields [44, 45, 48]. Farmers often use tillage practices to alter the soil structure near the surface [17], introducing hydrophobic material to the surface of a field and then applying tillage practices would potentially mix in the hydrophobic material. This would include hydrophobic material to the soil similar to the hydrophobic mixture experiment of this study but prevent a uniform layer of hydrophobic material that could potentially lead to runoff. A field study in a semi-arid climate would be a beneficial step as it would more closely model the evaporative conditions of the climate region of the Ogallala aquifer.

References

[1] "Water in Kansas," https://geokansas.ku.edu/water-kansas#:~:text=Almost%20all%20of%20the%20water,to%20pump%20the%20groundwater%20out.
[2] 2015, "Study finds High Plains Aquifer peak use by state, overall usage decline," https://www.k-state.edu/media/newsreleases/nov15/aquifer111615.html.
[3] 2020, "Kansas Climate," https://climate.k-state.edu/basics/.
[4] Araya, A., Kisekka, I., Gowda, P. H., and Prasad, P. V., 2017, "Evaluation of water-limited cropping systems in a semi-arid climate using DSSAT-CSM," Agricultural Systems, 150, pp. 86-98.
[5] Taghvaeian, S., Frazier, R. S., Livingston, D., and Fox, G., 2016, "Ogallala aquifer," Oklahoma Cooperative Extension Service.
[6] Scott, M., "National Climate Assessment: Great Plains' Ogallala Aquifer drying out," https://www.climate.gov/news-features/featured-images/national-climate-assessment-great-plains%E2%80%99-ogallala-aquifer-drying-out.
[7] "The Economic Contributions and Impacts of U.S. Food, Fiber, and Forest Industries," https://economic-impact-of-ag.uada.edu/kansas/.
[8] "Holcomb Station," https://sunflower.net/holcomb-station/.
[9] McGuire, V. L., "Change in Water in Storage in the High Plains Aquifer, Predevelopment to 2013," Proc. AGU Fall Meeting Abstracts, pp. H41G-0904.
[10] Mullan, D. J., and Reynolds, M. P., 2010, "Quantifying genetic effects of ground cover on soil water evaporation using digital imaging," Functional Plant Biology, 37(8), pp. 703-712.
[11] Schlesinger, W., 2018, "The fate of rainfall."
[12] Chakraborty, P. P., and Derby, M. M., "Contact line pinning and depinning prior to rupture of an evaporating droplet in a simulated soil pore," Proc. International Conference on Nanochannels, Microchannels, and Minichannels, American Society of Mechanical Engineers, p. V001T006A003.
[13] Chakraborty, P. P., Huber, R., Chen, X., and Derby, M. M., 2018, "Evaporation from simulated soil pores: effects of wettability, liquid islands, and breakup," Interfacial Phenomena and Heat Transfer, 6(4).
[14] Chakraborty, P. P., Ross, M., Bindra, H., and Derby, M. M., 2022, "Evaporative Drying from Hydrophilic or Hydrophobic Homogeneous Porous Columns: Consequences of Wettability, Porous Structure and Hydraulic Connectivity," Transport in Porous Media, 143(3), pp. 551-578.
[15] Shokri, N., Lehmann, P., and Or, D., 2008, "Effects of hydrophobic layers on evaporation from porous media," Geophysical Research Letters, 35(19).
[16] Shokri, N., Lehmann, P., and Or, D., 2009, "Characteristics of evaporation from partially wettable porous media," Water Resources Research, 45(2).
[17] Ochsner, T., Howerton, E., and Ellis, B., 2019, "Rain or Shine."
[18] Qiu, G. Y., and Ben-Asher, J., 2010, "Experimental determination of soil evaporation stages with soil surface temperature," Soil Science Society of America Journal, 74(1), pp. 13-22.
[19] Gutierrez, M. M., Cameron-Harp, M. V., Chakraborty, P. P., Stallbaumer-Cyr, E. M., Morrow, J. A., Hansen, R. R., and Derby, M. M., 2022, "Investigating a microbial approach to water conservation: Effects of Bacillus subtilis and Surfactin on evaporation dynamics in loam and sandy loam soils," Frontiers in Sustainable Food Systems, p. 441.

[20] Gupta, B., Shah, D., Mishra, B., Joshi, P., Gandhi, V. G., and Fougat, R., 2015, "Effect of top soil wettability on water evaporation and plant growth," Journal of colloid and interface science, 449, pp. 506-513.
[21] Wysocki, A., and Rieger, H., 2020, "Capillary action in scalar active matter," Physical Review Letters, 124(4), p. 048001.
[22] Jury, W., and Letey Jr, J., 1979, "Water vapor movement in soil: Reconciliation of theory and experiment," Soil Science Society of America Journal, 43(5), pp. 823-827.
[23] Davarzani, H., Smits, K., Tolene, R. M., and Illangasekare, T., 2014, "Study of the effect of wind speed on evaporation from soil through integrated modeling of the atmospheric boundary layer and shallow subsurface," Water resources research, 50(1), pp. 661-680.
[24] Knappett, J., and Craig, R. F., 2012, Craig's soil mechanics, CRC press.
[25] Hillel, D., 1998, Environmental Soil Physics, Academic Press.
[26] Cary, J., 1963, "ONSAGER'S RELATION AND THE NON-ISOTHERMAL DIFFUSION OF WATER VAPOR1," The Journal of Physical Chemistry, 67(1), pp. 126-129.
[27] Philip, J., and De Vries, D. d., 1957, "Moisture movement in porous materials under temperature gradients," Eos, Transactions American Geophysical Union, 38(2), pp. 222-232.
[28] Moldrup, P., Olesen, T., Gamst, J., Schjønning, P., Yamaguchi, T., and Rolston, D., 2000, "Predicting the gas diffusion coefficient in repacked soil water-induced linear reduction model," Soil Science Society of America Journal, 64(5), pp. 1588-1594.
[29] Lu, S., Ren, T., Yu, Z., and Horton, R., 2011, "A method to estimate the water vapour enhancement factor in soil," European Journal of Soil Science, 62(4), pp. 498-504.
[30] Cass, A., Campbell, G., and Jones, T., 1984, "Enhancement of thermal water vapor diffusion in soil," Soil Science Society of America Journal, 48(1), pp. 25-32.
[31] Hiraiwa, Y., and Kasubuchi, T., 2000, "Temperature dependence of thermal conductivity of soil over a wide range of temperature (5–75 C)," European Journal of Soil Science, 51(2), pp. 211-218.
[32] Pan, N., and Gibson, P., 2006, Thermal and moisture transport in fibrous materials, Woodhead Publishing.
[33] Hellwig, D., 1973, "Evaporation of water from sand, 4: The influence of the depth of the water-table and the particle size distribution of the sand," Journal of Hydrology, 18(3-4), pp. 317-327.
[34] An, N., Tang, C.-S., Xu, S.-K., Gong, X.-P., Shi, B., and Inyang, H. I., 2018, "Effects of soil characteristics on moisture evaporation," Engineering geology, 239, pp. 126-135.
[35] Lü, H., Yu, Z., Horton, R., Zhu, Y., Zhang, J., Jia, Y., and Yang, C., 2013, "Effect of gravel-sand mulch on soil water and temperature in the semiarid loess region of northwest China," Journal of hydrologic engineering, 18(11), pp. 1484-1494.
[36] Li, X.-Y., 2003, "Gravel–sand mulch for soil and water conservation in the semiarid loess region of northwest China," Catena, 52(2), pp. 105-127.
[37] Ding, J., Wu, J., Ding, D., Yang, Y., Gao, C., and Hu, W., 2021, "Effects of tillage and straw mulching on the crop productivity and hydrothermal resource utilization in a winter wheat-summer maize rotation system," Agricultural Water Management, 254, p. 106933.
[38] Dong, Z.-y., and Qian, B.-f., 2002, "Field investigation on effects of wheat-straw/corn-stalk mulch on ecological environment of upland crop farmland," Journal of Zhejiang University-SCIENCE A, 3, pp. 209-215.
[39] Robichaud, P., and Hungerford, R., 2000, "Water repellency by laboratory burning of four northern Rocky Mountain forest soils," Journal of Hydrology, 231, pp. 207-219.

[40] Hillel, D., 2013, Fundamentals of soil physics, Academic press.
[41] Chakraborty, P. P., 2022, "Evaporative drying from hydrophilic and hydrophobic single pores and porous media," Kansas State University.
[42] Truong, Q. H., Lee, J.-S., Dong, Y., and Yun, T. S., 2011, "Capillary induced small-strain stiffness for hydrophilic and hydrophobic granular materials: Experimental and numerical studies," Soils and foundations, 51(4), pp. 713-721.
[43] Da Re, G., Germaine, J. T., and Ladd, C. C., 2001, "Physical mechanisms controlling the pre-failure stress-strain behavior of frozen sand," MASSACHUSETTS INST OF TECH CAMBRIDGE DEPT OF CIVIL AND ENVIRONMENTAL ENGINEERING.
[44] DeBano, L. F., 1981, Water repellent soils: a state-of-the-art, US Department of Agriculture, Forest Service, Pacific Southwest Forest and ….
[45] Doerr, S. H., Shakesby, R., and Walsh, R., 2000, "Soil water repellency: its causes, characteristics and hydro-geomorphological significance," Earth-Science Reviews, 51(1-4), pp. 33-65.
[46] DeBano, L. F., 2000, "The role of fire and soil heating on water repellency in wildland environments: a review," Journal of hydrology, 231, pp. 195-206.
[47] Cerdà, A., and Doerr, S. H., 2007, "Soil wettability, runoff and erodibility of major dry-Mediterranean land use types on calcareous soils," Hydrological Processes: An International Journal, 21(17), pp. 2325-2336.
[48] Booker, F., Dietrich, W., and Collins, L., 1993, "Runoff and erosion after the Oakland firestorm," California Geology, 46(6), pp. 159-173.
[49] Bastidas, A. M. P., 2016, Ottawa F-65 sand characterization, University of California, Davis.
[50] Ichii, K., Uemura, K., Orai, N., and Hyodo, J., "Numerical simulation trial by cocktail glass model in FLIP ROSE for LEAP-UCD-2017," Proc. Model Tests and Numerical Simulations of Liquefaction and Lateral Spreading: LEAP-UCD-2017, Springer, pp. 611-627.
[51] Hudyma, N., and Avar, B. B., 2006, "Changes in swell behavior of expansive clay soils from dilution with sand," Environmental & Engineering Geoscience, 12(2), pp. 137-145.
[52] Kutter, B. L., Manzari, M. T., and Zeghal, M., 2019, Model tests and numerical simulations of liquefaction and lateral spreading: LEAP-UCD-2017, Springer Nature.
[53] Jeter, S., "Teaching the Principles and Practice of Uncertainty in the Undergraduate Laboratory," Proc. 2001 Annual Conference, pp. 6.959. 951-956.959. 958.
[54] Li, Z.-S., Mahmutovic, D., Fleureau, J.-M., Boutonnier, L., and Monnet, J., "Experimental and numerical approaches of the hydro-mechanical behaviour of a quasi-saturated compacted clayey soil," Proc. E3S Web of Conferences, EDP Sciences, p. 08015.
[55] Berthoz, N., Branque, D., Wong, H., and Subrin, D., 2013, "Stress measurement in partially saturated soils and its application to physical modeling of tunnel excavation," Canadian geotechnical journal, 50(10), pp. 1077-1087.
[56] Herring, T., Cey, E., and Pidlisecky, A., 2019, "Electrical resistivity of a partially saturated porous medium at subzero temperatures," Vadose Zone Journal, 18(1), pp. 1-11.
[57] McGaw, R., 1968, "Thermal conductivity of compacted sand/ice mixtures," Highway Research Record(215).
[58] Bergman, T. L., Bergman, T. L., Incropera, F. P., Dewitt, D. P., and Lavine, A. S., 2011, Fundamentals of heat and mass transfer, John Wiley & Sons.
[59] Bejan, A., 2013, Convection heat transfer, John wiley & sons.

[60] Jacobs, A., Verhoef, A., and de Bruin, H., 1996, "Sensible heat flux from sparse vegetation estimated using Nusselt numbers," Physics and Chemistry of the Earth, 21(3), pp. 107-110.
[61] Jacobs, A. F., and Verhoef, A., 1997, "Soil evaporation from sparse natural vegetation estimated from Sherwood numbers," Journal of Hydrology, 188, pp. 443-452.
[62] Gallego-Elvira, B., Baille, A., Martin-Gorriz, B., Maestre-Valero, J., and Martinez-Alvarez, V., 2012, "Evaluation of evaporation estimation methods for a covered reservoir in a semi-arid climate (south-eastern Spain)," Journal of hydrology, 458, pp. 59-67.
[63] Lee, C., and Wilke, C., 1954, "Measurements of vapor diffusion coefficient," Industrial & Engineering Chemistry, 46(11), pp. 2381-2387.
[64] Moran, M. J., Shapiro, H. N., Boettner, D. D., and Bailey, M. B., 2010, Fundamentals of engineering thermodynamics, John Wiley & Sons.
[65] Karim, M. Z., Tucker-Kulesza, S. E., and Derby, M. M., 2018, "Synthesizing hydrophobic sand and comparison of shear strength properties with hydrophilic sand," IFCEE 2018, pp. 75-83.